Hybrid Multiscale Integration for Directionally Scale Separable Problems

Shuhai Zhang* and Caglar Oskay†

Department of Civil and Environmental Engineering
Vanderbilt University
Nashville, TN 37235

Abstract

This manuscript presents the formulation and implementation of a hybrid multiscale integration scheme for multiscale problems that exhibit different scale separation characteristics in different directions. The proposed approach employs the key ideas of the variational multiscale enrichment at directions that exhibit poor scale separation and computational homogenization at directions with good scale separability. The proposed approach is particularly attractive for surface degradation problems in structures operating in the presence of aggressive environmental agents. Formulated in the context of variational multiscale principles, we develop a novel integration scheme that takes advantage of homogenization-like integration along directions that exhibit scale separation. The proposed integration scheme is applied to the reduced order variational multiscale enrichment (ROVME) method in order to arrive at a computationally efficient multiscale solution strategy for surface degradation problems. Numerical verifications are performed to verify the implementation of the hybrid multiscale integrator. The results of the verifications reveal high accuracy and computational efficiency, compared with the direct ROVME simulations. A coupled transport-thermo-mechanical analysis is presented to demonstrate the capability of the proposed computational framework.

Keywords: Multiscale modeling, Reduced order modeling, Variational multiscale enrichment, Computational homogenization, Hybrid multiscale integration.

---

*Department of Civil and Environmental Engineering, Vanderbilt University, Nashville, TN 37235, United States. Email: shuhai.zhang@vanderbilt.edu

†Corresponding author address: VU Station B#351831, 2301 Vanderbilt Place, Nashville, TN 37235. Email: caglar.oskay@vanderbilt.edu

1 Introduction

Structures operating in extreme environments subjected to high temperatures and thermo-mechanical loads often undergo surface degradation induced by the ingress of aggressive environmental agents. Examples of surface degradation include oxygen embrittlement of metal alloys in the structural components of high speed aircraft [41, 46], oxygen embrittlement of ceramic matrix composites [37], and hydrogen embrittlement of metals in hydrogen storage structures [19], among many others [29, 45]. While the aggressive agent ingress is often limited to a very small thickness along the exposed surfaces of the structure, materials properties changes within the affected regions are severe enough to cause significant reduction in strength and life of the overall structural component [35, 44]. This manuscript develops a computationally efficient, concurrent multiscale computational approach to address surface degradation problems.

Two categories of multiscale computational methods have emerged based on the concept of scale separability. Scale separation refers to the discrepancy between the characteristic size of the fine scale problem (i.e. the size of the heterogeneous representative volume or a unit cell, l_m) and that of the coarse scale problem (e.g., the dominant response feature such as the plastic process zone, l_M).

In the past few decades, a range of multiscale methods have been proposed to address those problems that operate at the limit of scale separation ($\zeta = l_m/l_M \to 0$). These include computational homogenization (also known as FE^2) [3, 23], multiscale finite element method [24, 18], heterogeneous multiscale method [17, 9], among others. In view of the tremendous computational complexity associated with coupled evaluation of problems at multiple scales, these methods are often employed in conjunction with reduced order modeling such as Fast Fourier transform [33], proper orthogonal decomposition [47], transformation field analysis [16, 12, 4, 32], eigendeformation-based homogenization (EHM) [40, 49, 50], machine learning based reduced modeling [8], hyper-reduced modeling [36], among others, particularly in the presence of nonlinear behavior.

Similarly, a number of global-local methods have been proposed to address problems that exhibit poor scale separation ($\zeta = l_m/l_M \approx 1$). The key idea in these approaches is to resolve the fine scale behavior at small subdomains of the overall structural domain, whereas a coarse description (e.g., a coarse discretization and phenomenological modeling) is employed within the remainder of the domain. Global-local finite element method [34, 31, 21, 22], domain decomposition methods [30], s-version finite elements [20], generalized finite elements [15], numerical subgrid algorithms [1, 2] based on the variational multiscale method [25, 27] among others are examples of global-local methods that employ this principle. More recently, the authors developed the variational multiscale enrichment (VME) method [38, 39, 48], a variant of the numerical subgrid algorithm, to study problems that exhibit material heterogeneity at the scale of the material microstructure. This approach relies on the resolution of the fine scale problems, which is computationally costly for large scale systems. The computational efficiency of the VME approach has been significantly improved by introducing a reduced order approximation of the fine scale response based on the EHM principles [40, 49, 50].

Surface degradation problems introduce a challenge to the existing multiscale computational methods, since they exhibit direction-dependent scale separability. In the direction normal to the exposed surfaces of the structure, aggressive agent ingress significantly alters the mechanical response and the resolution of the microstructural heterogeneities and the local response within this direction is critical to accurately assess the structural state. On the other hand, the response is self-similar along the transverse directions and the behavior could be accurately captured using the principles of computational homogenization.

This manuscript presents the formulation and implementation of a hybrid multiscale integration scheme for problems, where the relevant response fields exhibit different scale separation characteristics in various directions. The proposed approach employs the key ideas of the variational multiscale enrichment at directions, where the response fields exhibit poor scale separation, and the computational homogenization at directions, where the response fields show good scale separability. The formulation is based on the variational multiscale principles and develops a novel integration scheme that takes advantage of homogenization-like integration along directions that exhibit scale separation. The proposed integration scheme is also integrated with the reduced order variational multiscale enrichment in order to achieve a computationally efficient multiscale solution strategy for surface degradation problems. A suite of numerical verifications is performed to verify the implementation of the proposed multiscale scheme. The results of the verification studies indicate that the approach further improves the efficiency of the ROVME simulations, without significant compromise on accuracy. A coupled transport-thermo-mechanical analysis is presented to demonstrate the capability of the proposed computational framework.

The remainder of the manuscript is organized as follows: Section 2 provides the variational multiscale enrichment setting for directionally scale separable problems. The hybrid multiscale integration scheme is described in Section 3. Section 4 presents the application of the hybrid multiscale integration to the ROVME method. Section 5 details the hourglassing control of the proposed approach. Numerical verifications are presented in Section 6. In the context of small strains and elasto-viscoplastic constitutive behaviors, a coupled transport-thermo-mechanical problem with surface degradation is presented in Section 7 to demonstrate the capability of the proposed computational framework. Section 8 discusses the conclusions of this research.

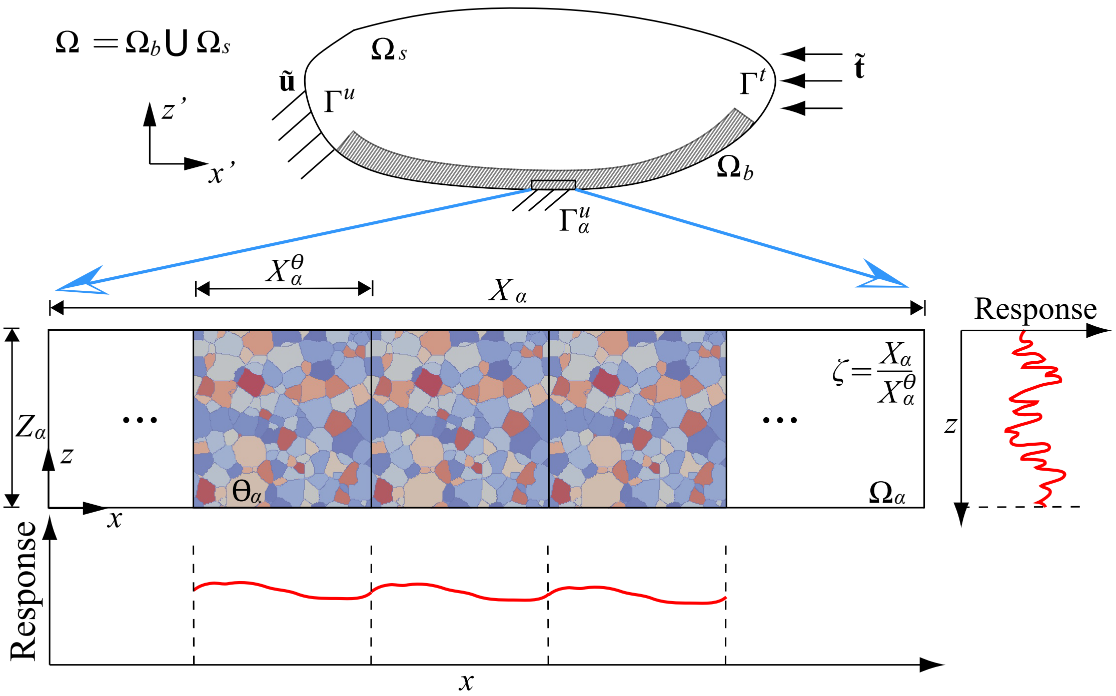

Figure 1: Domain decomposition for directionally scale separable problems

2 Variational multiscale enrichment setting for directionally scale separable problems

The proposed multiscale approach generalizes and builds on the variational multiscale enrichment idea introduced in Refs. [48, 49, 50]. Consider an open, bounded $\Omega \subset \mathbb{R}^2$ that constitutes the domain of the macroscopic structure. The global coordinate system is denoted by $\mathbf{x}' = (x', z')$ as shown in Fig. 1. Under the applied loading and environmental conditions, the structure undergoes significant localized deformation within a characteristic subdomain, $\Omega_b \in \Omega$, whereas within the remainder of the domain, $\Omega_s \equiv \Omega \backslash \Omega_b$, the response does not localize. We are therefore concerned with accurately and efficiently capturing response fields within Ω_b (i.e., the enrichment region). In surface degradation problems, the enrichment region spans the boundaries of the structure exposed to aggressive environmental agents but extends to a very limited depth compared to the overall structural thickness as illustrated in Fig. 1. The enrichment region is further discretized into a series of non-overlapping enrichment domains as:

$$\Omega_b = \bigcup_{\alpha=1}^{n_{\text{en}}} \Omega_\alpha; \quad \Omega_\alpha \cap \Omega_\beta \equiv \emptyset; \quad \alpha \neq \beta \tag{1}$$

in which, n_{en} denotes the total number of enrichment domains in the structure. The enrichment domain, Ω_α is formed by the repetition of a heterogeneous microstructure, Θ_α along the local direction, $x(\mathbf{x}')$ and the size of the microstructure is taken to be small compared to the dimension of the enrichment domain along the *homogenizable* direction, x. In contrast, the size of the enrichment domain in the normal direction $z(\mathbf{x}')$ is identical to that of the microstructure. The ratio between the size of the microstructure domain and the enrichment domain is denoted by a small positive scaling constant, ζ defined as:

$$\zeta = \frac{X_\alpha^\theta}{X_\alpha} \rightarrow 0 \tag{2}$$

in which, X_α^θ and X_α are the sizes of Θ_α and Ω_α in the x-direction, respectively. The response within the enrichment domain along x rapidly oscillates in space due to the fluctuations in the material properties within the microstructure. The response fields are therefore considered to be functions of the macroscale coordinate system, x, as well as a microscale coordinate system, $\breve{x} = x/\zeta$, which is a stretched position vector.

The problem setting described above indicates *directional homogenization* of the response fields; i.e., the response fields are scale separable at prescribed directions, whereas they are taken to be scale inseparable at other directions. We therefore seek to employ the computational homogenization principles along the scale separable directions, whereas employ the variational multiscale setting along the scale inseparable direction. Within this problem setting, an arbitrary response field in an enrichment domain is expressed as:

$$f^\zeta(\mathbf{x}) = f(x, \breve{x}(x), z) \tag{3}$$

where, f^ζ denotes the response field expressed in the original coordinate system, and superscript ζ indicates that the field is oscillatory in the scale separable direction.

We start by considering the following additive decomposition of the deformation field [27, 38, 48] within an arbitrary enrichment domain, Ω_α:

$$\mathbf{u}(x, \breve{x}, z, t) = \mathbf{u}^M(x, z, t) + \mathbf{u}_\alpha^m(x, \breve{x}, z, t) \tag{4}$$

where, $\mathbf{u}^M \in \mathcal{V}^M(\Omega)$ and $\mathbf{u}_\alpha^m \in \mathcal{V}_\alpha(\Omega_\alpha)$ are respectively the macroscale and microscale displacement fields; and $\mathcal{V}^M$ and $\mathcal{V}_\alpha$ denote the trial (discretized) spaces for the macro- and microscale fields, respectively:

$$\mathcal{V}^M(\Omega) \equiv \left\{ \mathbf{u}^M \left[x(\mathbf{x}'), z(\mathbf{x}'), t\right] \,\middle|\, \mathbf{u}^M = \sum_{A=1}^{N_D^\alpha} N_A(x', z')\ \hat{\mathbf{u}}_A^M(t); \right.$$
$$\left. \hat{\mathbf{u}}_A^M = \tilde{\mathbf{u}}(x'_A, z'_A, t) \text{ if } (x'_A, z'_A) \in \Gamma^u \right\} \tag{5}$$

$$\mathcal{V}_\alpha(\Omega_\alpha) \equiv \left\{ \mathbf{u}_\alpha^m(x, \breve{x}, z, t) \middle| \; \mathbf{u}_\alpha^m = \sum_{a=1}^{n_{d_\alpha}} n_{\alpha,a}(x, \breve{x}, z) \; \hat{\mathbf{u}}_{\alpha,a}^m(t); \; \hat{\mathbf{u}}_{\alpha,a}^m = 0 \text{ if } (x_\alpha, z_\alpha) \in \Gamma_\alpha^u \right\} \tag{6}$$

in which, $\tilde{\mathbf{u}}$ is the prescribed displacement along the Dirichlet boundary; N_D and n_{d_α} are the number of nodes associated with the finite element bases in the macro- and microscale discretizations, respectively; N_A and $n_{\alpha,a}$ are the shape functions for the macroscale and microscale fields, respectively; (x_A, z_A) and (x_α, z_α) are the corresponding nodal coordinates. Overhat denotes the nodal coefficients of the response field. The enrichment domains are taken to be geometrically simple such that each is represented by a single finite element in the macroscale grid. Homogeneous Dirichlet boundary conditions are employed along the enrichment domain boundaries to ensure displacement continuity across the enrichment domains [10]. The function fields are directly provided as discrete approximations and the formalism regarding the specialization from the continuum to discretized fields are skipped for brevity. The discrete approximations of the fine and coarse scale function spaces (and the corresponding fields) are, in fact, subspaces of the corresponding infinite dimensional Sobolev spaces with the usual smoothness and integrability conditions. It is important to note that the additive decomposition provided in Eq. (4) is admissible due to the direct sum decomposition property of the corresponding fine and coarse scale approximation spaces [27].

Following a similar decomposition to Eq. (4), the test function field is additively decomposed into macroscale ($\mathbf{w}^M$) and microscale ($\mathbf{w}_\alpha^m$) counterparts. Substituting the test and trial function decompositions into the governing equilibrium equations, and splitting the governing equations based on the micro- and macroscopic counterparts result in a coupled system of macroscale and microscale problems in the variational setting. The macroscale problem in the weak form yields:

Macroscale Problem:

$$\int_{\Omega_s} \nabla \mathbf{w}^M(x', z') : \boldsymbol{\sigma}(x', z', t) \; d\Omega + \sum_{\alpha=1}^{n_{\text{en}}} \int_{\Omega_\alpha} \nabla \mathbf{w}^M(x, z) : \boldsymbol{\sigma}(x, \breve{x}, z, t) \; d\Omega - \int_{\Gamma^t} \mathbf{w}^M(x', z') \cdot \tilde{\mathbf{t}}(x', z') \; d\Gamma = 0 \tag{7}$$

where, $\tilde{\mathbf{t}}$ is the prescribed traction along the Neumann boundary (Γ^t). The prescribed tractions are assumed to vary with the macroscopic coordinates only. The stress field is taken to be a local, history-dependent, nonlinear function of the strain and other internal state variables. Within each enrichment domain, the integration in Eq. (7) is expressed in the corresponding local coordinate system. Within the substrate region, the response is assumed to be unaffected by the material heterogeneity and accurately approximated by the macroscale response fields alone.

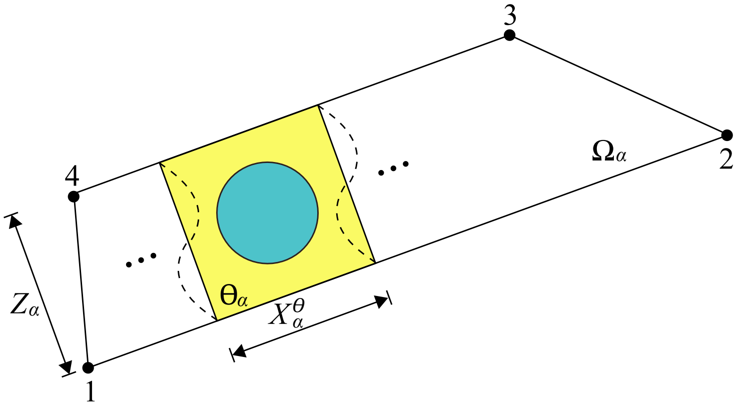

Figure 2: A macroscale enrichment domain for hybrid multiscale integration.

The weak form of the microscale problem at an arbitrary enrichment domain, Ω_α, is:

$$\textbf{Microscale Problem:} \quad \int_{\Omega_\alpha} \nabla \mathbf{w}_\alpha^m(x, \breve{x}, z) : \boldsymbol{\sigma}(x, \breve{x}, z, t) \; d\Omega = 0; \quad \alpha = 1, 2, ...n_{\text{en}}. \tag{8}$$

The microscale problems defined over each enrichment domain within the structure is tightly coupled to the macroscale problem. The coupling is through the stress terms in the respective equations which are functions of the total strain field that depends on the fine and coarse scale components of the displacement field. In the context of VME, the micro- and macroscale problems are evaluated in a coupled and iterative manner.

The evaluation of the coupled multiscale problem defined above is computationally expensive due to the complexity of the integral terms of the coarse and fine scale problems defined over the enrichment domains. The complexity is two-fold: (1) the microstructure is highly heterogeneous and exhibits highly nonlinear response that requires the evaluation of a large number of nonlinear enrichment domain problems in an iterative setting; and (2) within each enrichment domain, a large number of microstructures exist, over which the integrations must be performed. The latter difficulty was addressed through the development of the reduced order VME approach in Ref. [49]. In the current manuscript, we focus on developing a hybrid integration scheme in order to take advantage of the scale separability in select directions, and combining the hybrid integration scheme with the reduced order microstructure representation.

3 Hybrid Multiscale Integrator

Let the enrichment domain, Ω_α coincide with an element of the macroscale discretization within the enrichment region. The shape of the enrichment domain is constrained due to the directional scale separation condition: (1) considering a microstructure with an aspect ratio of O(1), the aspect ratio of the enrichment domain is taken to be high; and (2) the element length in the scale inseparable direction is taken to be constant and equal to the edge length of the microstructure along the same direction. Define vectors $\mathbf{v}_{ij} = \mathbf{x}'_j - \mathbf{x}'_i = (x'_j, z'_j) - (x'_i, z'_i)$; $i, j = 1, 2, 3, 4$; $i \neq j$ within the enrichment domain. Denoting the size of the microstructure in the scale separable direction as X_α^θ and in the scale inseparable direction as Z_α^θ, the above-mentioned constraints are imposed as follows:

(i) $\mathbf{v}_{12}//\mathbf{v}_{34}$ (i.e., $|(\mathbf{v}_{12} \cdot \mathbf{v}_{34})/(||\mathbf{v}_{12}||\ ||\mathbf{v}_{34}||)| = 1$), and;

$$\zeta = \frac{2X_\alpha^\theta}{\parallel \mathbf{v}_{12} \parallel + \parallel \mathbf{v}_{34} \parallel} \rightarrow 0; \qquad Z_\alpha^\theta = Z_\alpha \equiv |\mathbf{v}_{23} \cdot \mathbf{v}_n| \tag{9}$$

where, $\mathbf{v}_n \perp \mathbf{v}_{12}$ and $\mathbf{v}_n$ is a unit vector, or;

(ii) $\mathbf{v}_{23}//\mathbf{v}_{41}$ (i.e., $|(\mathbf{v}_{23} \cdot \mathbf{v}_{41})/(||\mathbf{v}_{23}||\ ||\mathbf{v}_{41}||)| = 1$), and;

$$\zeta = \frac{2X_\alpha^\theta}{\parallel \mathbf{v}_{23} \parallel + \parallel \mathbf{v}_{41} \parallel} \rightarrow 0; \qquad Z_\alpha^\theta = Z_\alpha \equiv |\mathbf{v}_{12} \cdot \mathbf{v}_n|; \qquad \mathbf{v}_n \perp \mathbf{v}_{23}. \tag{10}$$

where, $(\cdot)//(*)$ indicates $(\cdot)$ parallels to $(*)$, $\parallel (\cdot) \parallel$ denotes the norm of a vector $(\cdot)$ and $|(*)|$ is the absolute value of a scalar $(*)$. When (i) or (ii) is satisfied, such as in the example shown in Fig. 2, the enrichment domain is scale separable, and the hybrid multiscale integration scheme described below is applicable.

3.1 Canonical coordinate systems

In context of standard finite element coordinate system transformation, the macroscale problem for an enrichment domain is first transfered from the global coordinate system ($\mathbf{x}'$) to a standard canonical system ($\boldsymbol{\xi}$). Then, the response discretization in Eq. (5) is performed using the standard shape functions in the canonical system. In the current setting, a new set of canonical systems, as illustrated in Fig. 3, and the associated shape functions are employed. The canonical system of the enrichment domain, Ω_α, is denoted as $\square_\xi$ with the associated limits as $\xi \in [-1/\zeta, 1/\zeta]$ and $\eta \in [-1, 1]$. Embedded in the enrichment domain, $\square$ denotes the canonical system for the microstructure, Θ_α, which resolves the microstructural material heterogeneity, as illustrated in Fig. 3. Its limits are $\breve{\xi} \in [-1, 1]$ and $\eta \in [-1, 1]$. The two systems have separate coordinates in the scale separable ξ-direction, but share the same coordinate in the η-direction. In the absence of resolved microstructural topology, $\square$ is identical to the standard canonical system with the standard shape functions. New shape functions are

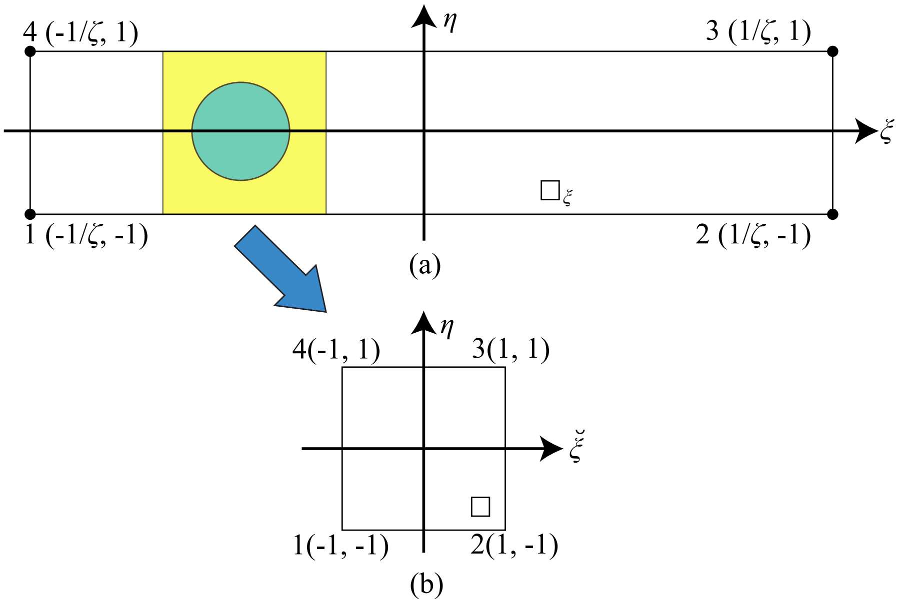

Figure 3: Canonical systems of the hybrid integration for: (a) the enrichment domain and (b) the microstructure of the enrichment domain.

defined for $\square_\xi$ as:

$$
\begin{aligned}
N_1(\xi,\eta;\zeta) &= \frac{(1-\zeta\ \xi)(1-\eta)}{4}; \qquad N_2(\xi,\eta;\zeta) = \frac{(1+\zeta\ \xi)(1-\eta)}{4} \\
N_3(\xi,\eta;\zeta) &= \frac{(1+\zeta\ \xi)(1+\eta)}{4}; \qquad N_4(\xi,\eta;\zeta) = \frac{(1-\zeta\ \xi)(1+\eta)}{4}.
\end{aligned}
\tag{11}
$$

The hybrid integrations for the micro- and macroscale problems over the enrichment domains are performed by considering the canonical systems in Fig. 3 and their shape functions.

3.2 Integration of macroscale and microscale problems

We first demonstrate the proposed hybrid multiscale integration over a scalar function, ψ. The integration scheme is then applied to the enrichment domain integrals that appear in the microscale and macroscale problems. Let ψ be sufficiently smooth and integrable function over the enrichment domain. The function is assumed to be periodic along the homogenizable direction, x. Considering coordinate transformation and the homogenization concept in the ξ-direction as $\zeta \rightarrow 0$ [23], the integration of ψ over Ω_α is expressed as follows:

$$
\begin{aligned}
\lim_{\zeta\rightarrow 0} \int_{\Omega_\alpha} \psi(x, \breve{x} = \frac{x}{\zeta}, z)\ d\Omega &= \lim_{\zeta\rightarrow 0} \int_{-1}^{1} \int_{-\frac{1}{\zeta}}^{\frac{1}{\zeta}} \psi(\xi, \breve{\xi}, \eta)\ \det J(\xi,\eta)\ d\xi\ d\eta \\
&= \int_{-1}^{1} \int_{-\frac{1}{\zeta}}^{\frac{1}{\zeta}} \bar{\psi}(\xi,\eta)\ \det J(\xi,\eta)\ d\xi\ d\eta
\end{aligned}
\tag{12}
$$

where, $\int_{-1}^{1}\int_{-\frac{1}{\zeta}}^{\frac{1}{\zeta}} f(\xi,\breve{\xi},\eta)\ d\xi d\eta = \int_{\square_\zeta} f(\xi,\breve{\xi},\eta)\ d\xi d\eta$ is the integration over the canonical domain of the enrichment domain (Fig. 3 (a)), $J(\xi,\eta)$ is the Jacobian matrix for the coordinate transformation, $\det(\cdot)$ denote the determinant, and $\bar{\psi}$ is the microstructure-average (i.e., homogenized) function along the homogenizable direction which is defined as:

$$\bar{\psi}(\xi,\eta) = \frac{1}{2}\int_{-1}^{1} \psi(\xi,\breve{\xi},\eta)\ d\breve{\xi}. \tag{13}$$

The integration shown in Eq. (12) at the homogenization limit exists and is convergent (assuming the standard continuity and periodicity requirements for ψ), since it is identical to the weak convergence argument of the mathematical homogenization theory [6, 13] - but only applied to a single direction. Employing the one-dimensional Gaussian quadrature rule and approximating the integration of the homogenized response ($\bar{\psi}$) in the ξ-direction with ng integration points:

$$\int_{-\frac{1}{\zeta}}^{\frac{1}{\zeta}} \bar{\psi}(\xi,\eta)\ \det J(\xi,\eta)\ d\xi \approx \sum_{g=1}^{ng} \bar{\psi}(\xi_g,\eta)\ \det J(\xi_g,\eta)\ \mathcal{W}_g; \quad \text{and } g = 1,2,...,ng \tag{14}$$

where, $\int_{-\frac{1}{\zeta}}^{\frac{1}{\zeta}} f(\xi,\breve{\xi},\eta)\ d\xi$ is the integration over the scale separable direction of the canonical domain of an enrichment domain (the ξ-direction of Fig. 3 (a)), $\xi_g = \bar{\xi}_g/\zeta$ indicates the position of the Gaussian quadrature point in the ξ-direction and $\mathcal{W}_g = \bar{\mathcal{W}}_g/\zeta$ is the corresponding weight. $\bar{\xi}_g$ and $\bar{\mathcal{W}}_g$ are the positions and weights of the standard Gaussian quadrature points for $\xi \in [-1,1]$, respectively. Substituting Eq. (14) into Eq. (12), the integration over the enrichment domain is approximated as:

$$\lim_{\zeta\to 0}\int_{\Omega_\alpha} \psi(x,\breve{x}=\frac{x}{\zeta},z)\ d\Omega \approx \sum_{g=1}^{ng}\int_{-1}^{1} \bar{\psi}(\xi_g,\eta)\ \det J(\xi_g,\eta)\ d\eta\ \mathcal{W}_g. \tag{15}$$

Considering Eq. (13) and defining $\int_{\square} f(\xi_g,\breve{\xi},\eta)\ d\breve{\Omega} \equiv \int_{-1}^{1}\int_{-1}^{1} f(\xi_g,\breve{\xi},\eta)\ d\breve{\xi} d\eta$, the hybrid integration over an enrichment domain yields:

$$\lim_{\zeta\to 0}\int_{\Omega_\alpha} \psi(x,\breve{x}=\frac{x}{\zeta},z)\ d\Omega \approx \sum_{g=1}^{ng}\frac{\mathcal{W}_g}{2}\int_{\square} \psi(\xi_g,\breve{\xi},\eta)\ \det J(\xi_g,\eta)\ d\breve{\Omega}. \tag{16}$$

Equation (16) is the general hybrid integration rule which can be applied to any integrable function over an enrichment domain in directionally scale separable problems.

Applying the hybrid multiscale integration approach to the integration over an arbitrary enrichment domain of the macroscale problem (Eq. (7)) yields the following expression:

$$\begin{aligned} &\lim_{\zeta \to 0} \int_{\Omega_\alpha} \nabla \mathbf{w}^M(x,z) : \boldsymbol{\sigma}(x,\breve{x},z,t)\ d\Omega \\ &\qquad \approx \sum_{g=1}^{ng} \frac{\mathcal{W}_{\alpha g}}{2} \int_{\square} \nabla \mathbf{w}^M(\xi_{\alpha g},\eta) : \boldsymbol{\sigma}(\xi_{\alpha g},\breve{\xi},\eta,t)\ \det J(\xi_{\alpha g},\eta)\ d\breve{\Omega} \end{aligned} \tag{17}$$

where, $\xi_{\alpha g}$ and $\mathcal{W}_{\alpha g}$ are the positions and associated weights for the enrichment domain, Ω_α. Similarly, the microscale weak form for the enrichment domain Ω_α (Eq. (8)) is obtained as:

$$\begin{aligned} &\lim_{\zeta \to 0} \int_{\Omega_\alpha} \nabla \mathbf{w}^m_\alpha(x,\breve{x},z) : \boldsymbol{\sigma}(x,\breve{x},z,t)\ d\Omega \\ &\qquad \approx \sum_{g=1}^{ng} \frac{\mathcal{W}_{\alpha g}}{2} \int_{\square} \nabla \mathbf{w}^m_\alpha(\xi_{\alpha g},\breve{\xi},\eta) : \boldsymbol{\sigma}(\xi_{\alpha g},\breve{\xi},\eta,t)\ \det J(\xi_{\alpha g},\eta)\ d\breve{\Omega} = 0. \end{aligned} \tag{18}$$

Since $\mathcal{W}_{\alpha g}$ does not depend on $\breve{\xi}$ or η, a solution that ensures the equilibrium of the microscale state (Eq. (18)) is:

$$\int_{\square} \nabla \mathbf{w}^m_\alpha(\xi_{\alpha g},\breve{\xi},\eta) : \boldsymbol{\sigma}(\xi_{\alpha g},\breve{\xi},\eta,t)\ \det J(\xi_{\alpha g},\eta)\ d\breve{\Omega} = 0; \qquad \forall g = 1,2,...,ng. \tag{19}$$

Equation (19) implies that under the condition of directional scale-separability, enforcement of equilibrium at the scale of the microstructure associated with each quadrature point implies the microscale equilibrium within the enrichment domain. Equations (18) and (19)) represent the integration over an arbitrary enrichment domain (Eq. (7)) which consists of: 1) a two-scale integration along the scale separable direction ($\xi_{\alpha g}$ and ξ represents macroscale and microscale, respectively); and 2) a single scale integration (η) performed along the scale inseparable direction. The application of the hybrid multiscale integration to the micro- and macroscale problems requires that the fine scale components of the response fields over the microstructure are periodic along the η-direction. In order to ensure continuity across neighboring enrichment domains or along the boundaries between the enrichment domains and the substrate [38, 48], homogeneous Dirichlet boundary conditions are prescribed for microstructure boundaries along the $\breve{\xi}$-direction, as illustrated in Fig. 4.

4 Hybrid Integration for Reduced Order Variational Multiscale Enrichment (HROVME)

In this section, we describe the application of the proposed hybrid multiscale integration approach to the reduced order variational multiscale enrichment (ROVME) method for elasto-

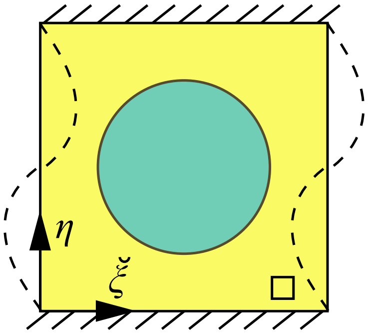

Figure 4: Boundary conditions for the microstructures.

viscoplastic problems. The ROVME method, recently proposed by the authors [49, 50], approximates the nonlinear heterogeneous response within the enrichment domain using a reduced approximation basis to enhance the computational efficiency. ROVME is applicable when the microstructure domain and the enrichment domain coincides (i.e., when ζ=1). By applying the proposed hybrid multiscale integrator to ROVME (referred to as HROVME in what follows), we aim to address directionally scale separable problems (i.e., when $\zeta = 0$) in an efficient manner.

4.1 The microscale problem

The microscale problem as stated in Eq. (19) is numerically evaluated through ROVME. Considering Eq. (4) and the canonical systems of the hybrid multiscale integration, the constitutive equation at a fixed $\xi_{\alpha g}$ is expressed as:

$$\boldsymbol{\sigma}(\xi_{\alpha g},\breve{\xi},\eta,t) = \mathbf{L}^{\alpha}(\breve{\xi},\eta) : \Big[\nabla\mathbf{u}^{M}(\xi_{\alpha g},\eta,t) + \nabla\mathbf{u}^{m}_{\alpha}(\xi_{\alpha g},\breve{\xi},\eta,t) - \boldsymbol{\varepsilon}^{vp}(\xi_{\alpha g},\breve{\xi},\eta,t)\Big] \tag{20}$$

where, $\mathbf{L}^{\alpha}$ is the tensor of elastic moduli which varies spatially within the microstructure; $\boldsymbol{\varepsilon}^{vp}$ denote the viscoplastic strain. By this expression, the additive split of the total strain tensor to elastic and inelastic counterparts is assumed for the constitutive laws of the material constituents. Employing the ROVME idea [49, 50], the microscale displacement field is expressed as:

$$\mathbf{u}^{m}_{\alpha}(\xi_{\alpha g},\breve{\xi},\eta,t) = \sum_{A=1}^{N^{\alpha}_{D}} \mathbf{H}^{\alpha g}_{A}(\breve{\xi},\eta,\zeta)\cdot\hat{\mathbf{u}}^{M\alpha}_{A}(t) + \int_{\square} \mathbf{h}^{\alpha}(\breve{\xi},\eta,\hat{\xi},\hat{\eta}) : \boldsymbol{\varepsilon}^{vp}(\xi_{\alpha g},\hat{\xi},\hat{\eta},t)\; d\hat{\Omega} \tag{21}$$

where, $\hat{\Omega} = (\hat{\xi},\hat{\eta}) \in \square$; N^{α}_{D} is the number of nodes of the macroscale element associated with the enrichment domain; $\mathbf{H}^{\alpha g}_{A}$ is the elastic influence function associated with the g^{th} integration point of the enrichment domain; and $\mathbf{h}^{\alpha}$ is the inelastic influence function induced by the inelastic behavior within the microstructure. The influence functions are approximations to Green's function problems defined over the microstructure, and evaluated numerically. With a slight deviation from the ROVME approach, the influence functions are evaluated by considering the semi-periodic boundary conditions described above. Considering element level discretization of the macroscale displacement field through the ζ-dependent shape functions in Eq. (11):

$$\mathbf{u}^{M}(\xi_{\alpha g}, \eta, t) = \sum_{A=1}^{N_D^{\alpha}} N_A(\xi_{\alpha g}, \eta, \zeta, t)\ \hat{\mathbf{u}}_A^{M\alpha}(t) \tag{22}$$

and, substituting the constitutive equation (Eq. (20)), macro- and microscale displacement discretizations (Eqs. (21) and (22)) into Eq. (19), the microscale problem in weak form yields:

$$\begin{aligned} \sum_{A=1}^{N_D^{\alpha}} \Bigg[\int_{\square} & \nabla \mathbf{w}_{\alpha g}^{m}(\breve{\xi}, \eta) : \mathbf{L}^{\alpha}(\breve{\xi}, \eta) \cdot \nabla N_A(\xi_{\alpha g}, \eta, \zeta)\ \mathrm{det}J(\xi_{\alpha g}, \eta)\ d\breve{\Omega} \\ & + \int_{\square} \nabla \mathbf{w}_{\alpha g}^{m}(\breve{\xi}, \eta) : \mathbf{L}^{\alpha}(\breve{\xi}, \eta) : \nabla \mathbf{H}_A^{\alpha g}(\breve{\xi}, \eta, \zeta)\ \mathrm{det}J(\xi_{\alpha g}, \eta)\ d\breve{\Omega} \Bigg] \cdot \hat{\mathbf{u}}_A^{M\alpha}(t) \\ & + \int_{\square} \nabla \mathbf{w}_{\alpha g}^{m}(\breve{\xi}, \eta) : \mathbf{L}^{\alpha}(\breve{\xi}, \eta) : \Bigg[\int_{\square} \nabla \mathbf{h}^{\alpha}(\breve{\xi}, \eta, \hat{\xi}, \hat{\eta}) : \boldsymbol{\varepsilon}^{vp}(\xi_{\alpha g}, \hat{\xi}, \hat{\eta}, t)\ d\hat{\Omega} \\ & \qquad - \boldsymbol{\varepsilon}^{vp}(\xi_{\alpha g}, \breve{\xi}, \eta, t) \Bigg]\ \mathrm{det}J(\xi_{\alpha g}, \eta)\ d\breve{\Omega} = 0 \end{aligned} \tag{23}$$

where, $\nabla \mathbf{w}_{\alpha g}^{m}(\breve{\xi}, \eta) \equiv \nabla \mathbf{w}_{\alpha}^{m}(\xi_{\alpha g}, \breve{\xi}, \eta)$. Considering the case when the microstructure deforms elastically ($\boldsymbol{\varepsilon}^{vp} = 0$), Eq. (23) yields the elastic influence function problem that can be solved for $\mathbf{H}_A^{\alpha g}$:

$$\begin{aligned} \int_{\square} & \nabla \mathbf{w}_{\alpha g}^{m}(\breve{\xi}, \eta) : \mathbf{L}^{\alpha}(\breve{\xi}, \eta) : \nabla \mathbf{H}_A^{\alpha g}(\breve{\xi}, \eta, \zeta)\ \mathrm{det}J(\xi_{\alpha g}, \eta)\ d\breve{\Omega} = \\ & - \int_{\square} \nabla \mathbf{w}_{\alpha g}^{m}(\breve{\xi}, \eta) : \mathbf{L}^{\alpha}(\breve{\xi}, \eta) \cdot \nabla N_A(\xi_{\alpha g}, \eta, \zeta)\ \mathrm{det}J(\xi_{\alpha g}, \eta)\ d\breve{\Omega}; \\ & \forall A = 1, 2, ..., N_D^{\alpha} \ \text{ and } \ g = 1, 2, ..., ng. \end{aligned} \tag{24}$$

Substituting Eq. (24) into the microscale weak form (Eq. (23)), results in the inelastic influence function problem for $\mathbf{h}^{\alpha}$:

$$\begin{aligned} \int_{\square} & \nabla \mathbf{w}_{\alpha g}^{m}(\breve{\xi}, \eta) : \mathbf{L}^{\alpha}(\breve{\xi}, \eta) : \nabla \mathbf{h}^{\alpha}(\breve{\xi}, \eta, \hat{\xi}, \hat{\eta})\ \mathrm{det}J(\xi_{\alpha g}, \eta)\ d\breve{\Omega} = \\ & \int_{\square} \nabla \mathbf{w}_{\alpha g}^{m}(\breve{\xi}, \eta) : \mathbf{L}^{\alpha}(\breve{\xi}, \eta)\ \delta^{d}(\breve{\xi} - \hat{\xi}, \eta - \hat{\eta})\ \mathrm{det}J(\xi_{\alpha g}, \eta)\ d\breve{\Omega}; \quad \forall (\hat{\xi}, \hat{\eta}) \in \square \end{aligned} \tag{25}$$

in which, δ^{d} denotes the Dirac delta distribution. The elastic and inelastic microscale influence function problems are linear elastic problems defined over the microstructure. Therefore, the influence functions are computed off-line, prior to a macroscale analysis.

Next, a microstructure partitioning is considered to obtain a reduced order approximation to the microscale problems [40, 49, 50]. The microstructure defined in the canonical form is decomposed into NP non-overlapping subdomains (i.e., parts):

$$\square = \bigcup_{\gamma=1}^{NP} \square_\gamma; \quad \square_\gamma \cap \square_\lambda \equiv \emptyset \ \text{ when } \ \gamma \neq \lambda \tag{26}$$

where, $\square_\gamma$ denotes a part of the microstructure. Stress and inelastic strain fields within the microstructure are then expressed as:

$$\boldsymbol{\sigma}(\xi_{\alpha g}, \breve{\xi}, \eta, t) = \sum_{\gamma=1}^{NP} \hat{N}_\gamma(\breve{\xi}, \eta) \ \boldsymbol{\sigma}_\gamma^{\alpha g}(t); \qquad \boldsymbol{\varepsilon}^{vp}(\xi_{\alpha g}, \breve{\xi}, \eta, t) = \sum_{\gamma=1}^{NP} \hat{N}_\gamma(\breve{\xi}, \eta) \ \boldsymbol{\mu}_\gamma^{\alpha g}(t) \tag{27}$$

where, $\hat{N}_\gamma(\breve{\xi}, \eta)$ denotes a reduced model shape function:

$$\hat{N}_\gamma(\breve{\xi}, \eta) = \begin{cases} 1, & \text{if } (\breve{\xi}, \eta) \in \square_\gamma \\ 0, & \text{elsewhere .} \end{cases} \tag{28}$$

The stress and inelastic strain fields are therefore approximated as spatially piecewise constant fields with unknown coefficients , $\boldsymbol{\sigma}_\gamma^{\alpha g}$ and $\boldsymbol{\mu}_\gamma^{\alpha g}$, respectively. Substituting Eq. (27) into Eq. (20) and using Eq. (28), the constitutive equation is expressed in terms of the unknown stress and inelastic coefficients as:

$$\boldsymbol{\sigma}_\lambda^{\alpha g}(t) = \sum_{A=1}^{N_D^\alpha} \mathbf{S}_{\lambda A}^{\alpha g}(\zeta) \cdot \hat{\mathbf{u}}_A^{M\alpha}(t) + \sum_{\gamma=1}^{NP} \mathbf{P}_{\lambda\gamma}^{\alpha} : \boldsymbol{\mu}_\gamma^{\alpha g}(t) \tag{29}$$

where,

$$\mathbf{S}_{\lambda A}^{\alpha g}(\zeta) = \frac{1}{|\Theta_\lambda^\alpha|} \int_{\Theta_\lambda^{\alpha g}} \left[\mathbf{L}^\alpha(\breve{\xi}, \eta) \cdot \nabla N_A(\xi_{\alpha g}, \eta, \zeta) + \mathbf{L}^\alpha(\breve{\xi}, \eta) : \nabla \mathbf{H}_A^{\alpha g}(\breve{\xi}, \eta, \zeta) \right] \, d\Omega \tag{30}$$

$$\mathbf{P}_{\lambda\gamma}^{\alpha} = \frac{1}{|\Theta_\lambda^\alpha|} \int_{\Theta_\lambda^{\alpha g}} \left[\mathbf{L}^\alpha(\breve{\xi}, \eta) : \int_{\Theta_\gamma^{\alpha g}} \nabla \mathbf{h}^\alpha(\breve{\xi}, \eta, \hat{\xi}, \hat{\eta}) \, d\hat{\Omega} - \mathbf{L}^\alpha(\breve{\xi}, \eta) \ \hat{N}_\gamma(\breve{\xi}, \eta) \right] \, d\Omega. \tag{31}$$

Equation (29) along with the evolution equations for viscoplastic slip defined for inelastic strain coefficients ($\boldsymbol{\mu}_\gamma^{\alpha g}$) constitute a nonlinear, history dependent system of equations that are evaluated for the inelastic strain and stress coefficients for a prescribed macroscopic deformation state ($\mathbf{u}^{M\alpha}$) within the enrichment domain.

Remark 1. The reduced basis approximation of the microscale problem has the following characteristics: (1) The order of the reduced basis is of NP. The number of parts is taken to be much smaller compared to the number of degrees of freedom in a typical finite element discretization of the microstructure domain. (2) The coefficient tensors ($\mathbf{S}$ and $\mathbf{P}$) are functions of the elastic properties of the microstructure constituents, the influence functions ($\mathbf{H}$ and $\mathbf{h}$), and the scaling parameter, ζ, as shown in Eqs. (30) and (31). For a fixed scaling constant, the coefficient tensors are therefore computable a-priori, similar to the influence functions. In contrast, macroscopic discretization could include enrichment domains with varying element lengths (i.e., varying scaling constants). The Appendix provides an analytical relationship for computing the coefficient tensors for an arbitrary scaling constant from those pre-computed for a reference scaling constant. This analytical relationship is significant, since by this approach, a single set of coefficient tensors is stored for all enrichment domains regardless of shape.

4.2 The macroscale problem

Consider the component of the macroscale problem defined in Eq. (7) for the enrichment domain, Ω_α:

$$\tilde{\Phi}_\alpha^M \equiv \int_{\Omega_\alpha} \nabla \mathbf{w}^M(x,z) : \boldsymbol{\sigma}(x,\breve{x},z,t)\; d\Omega. \tag{32}$$

Using the standard Bubnov-Galerkin approach, the macroscale test function is discretized in the local coordinate system of the enrichment domain:

$$\mathbf{w}^M(x,z) = \sum_{A=1}^{N_D^\alpha} N_A(x,z)\; \hat{\mathbf{w}}_A^{M\alpha}. \tag{33}$$

Employing the Voigt notation (vector-matrix form), Eq. (32) is rewritten as:

$$\tilde{\Phi}_\alpha^M = \left(\hat{\mathbf{w}}^{M\alpha}\right)^T \tilde{\boldsymbol{\Psi}}_\alpha^M \tag{34}$$

where,

$$\hat{\mathbf{w}}^{M\alpha} = \left[\hat{\mathbf{w}}_A^{M\alpha}\right]_{A\in[1,N_D^\alpha]} \tag{35}$$

and

$$\tilde{\boldsymbol{\Psi}}_\alpha^M = \int_{\Omega_\alpha} \mathbf{B}^T(x,z)\; \boldsymbol{\sigma}\left(x,\breve{x},z,t\right)\; d\Omega \tag{36}$$

in which, $\mathbf{B}$ is in the form of the standard gradient of shape functions tensor. Considering the hybrid integration (Eq. (16)) and the reduced order approximation of the stress tensor (Eq. (27)), the matrix form of the macroscale weak form yields:

$$\tilde{\boldsymbol{\Psi}}_\alpha^M \approx \sum_{g=1}^{ng} \frac{\mathcal{W}_{\alpha g}}{2} \int_{\square} \mathbf{B}^T(\xi_{\alpha g},\eta,\zeta)\; \boldsymbol{\sigma}(\xi_{\alpha g},\breve{\xi},\eta,t)\; \det J(\xi_{\alpha g},\eta)\; d\breve{\Omega} = \sum_{g=1}^{ng}\; \left[\mathbf{B}^{\alpha g}(\zeta)\right]^T\; \boldsymbol{\sigma}^{\alpha g} \tag{37}$$

where,

$$\mathbf{B}^{\alpha g}(\zeta) = \left[\mathbf{B}^{\alpha g}_{\gamma}(\zeta)\right]_{\gamma \in [1,NP]}; \qquad \mathbf{B}^{\alpha g}_{\gamma}(\zeta) = \frac{\mathcal{W}_{\alpha g}}{2} \int_{\square_\gamma} \mathbf{B}(\xi_{\alpha g}, \eta, \zeta) \; \det J(\xi_{\alpha g}, \eta) \; d\breve{\Omega} \tag{38}$$

and

$$\boldsymbol{\sigma}^{\alpha g} = \left[\boldsymbol{\sigma}^{\alpha g}_{\gamma}(t)\right]_{\gamma \in [1,NP]}. \tag{39}$$

Similar to the coefficient tensors **S** and **P**, **B** is a function of the scaling constant, ζ. By employing the relationship shown in the Appendix, **B** for an arbitrary scaling constant is evaluated directly from a **B** matrix pre-computed for a reference scaling constant.

Considering the discretization of the macroscale weak form over the entire macroscopic domain (Eq. (7)), the macrocale system of equations in the global coordinate system is defined as:

$$\boldsymbol{\Psi}'^{M} \equiv \underset{e}{\mathbf{A}} \, \boldsymbol{\Psi}'^{M}_{e} = 0; \qquad \forall \; \Omega_e \in \Omega \tag{40}$$

where, $\mathbf{A}$ is the standard finite element assembly operator. For each enrichment domain, $\Omega_e \in \{\Omega_\alpha | \alpha = 1, 2, ..., n_{\text{en}}\}$, the residual in the global coordinate system is obtained from that defined in the local coordinate system of the enrichment domain:

$$\boldsymbol{\Psi}'^{M}_{e} = \boldsymbol{\Psi}'^{M}_{\alpha} = \mathbf{R} \; \boldsymbol{\Psi}^{M}_{\alpha}; \qquad \Omega_e \in \Omega_\alpha(\alpha = 1, 2, ..., n_{\text{en}}) \tag{41}$$

in which, **R** is the coordinate rotation tensor between the enrichment domain ($\mathbf{x}$) and the global coordinate system ($\mathbf{x}'$). The residual of the macroscale weak form in the local coordinate system is expressed as:

$$\boldsymbol{\Psi}^{M}_{\alpha} \equiv \tilde{\boldsymbol{\Psi}}^{M}_{\alpha} - \tilde{\boldsymbol{\Psi}}^{MT}_{\alpha} \tag{42}$$

where, $\tilde{\boldsymbol{\Psi}}^{M}_{\alpha}$ is described in Eq. (37) and:

$$\tilde{\boldsymbol{\Psi}}^{MT}_{\alpha} = \int_{\Gamma^t_\alpha} \mathbf{N}^{M}(x, z) \cdot \tilde{\mathbf{t}} \; d\Gamma \tag{43}$$

where, $\mathbf{N}^M$ denotes the standard shape function matrix in Voigt notation. Γ^t_α is the part of the enrichment domain boundary that intersects with the Neumann boundary of the problem domain ($\Gamma^t_\alpha \equiv \Gamma_\alpha \cap \Gamma^t$), in the absence of the microscale displacement field contribution. For macroscale elements that discretize the substrate region ($\Omega_e \in \Omega_s$), the residual of the macroscale weak form is expressed as:

$$\boldsymbol{\Psi}'^{M}_{e} = \boldsymbol{\Psi}'^{M}_{s} \equiv \tilde{\boldsymbol{\Psi}}'^{M}_{s} - \tilde{\boldsymbol{\Psi}}'^{MT}_{s}; \qquad \Omega_e \in \Omega_s \tag{44}$$

Table 1: Rank of the element stiffness matrix for the heterogeneous microstructure.

Partition	(a)	(b)	(c)	(d)	(e)	(f)	(g)	(h)
Rank of the element stiffness matrix	3	3	3	3	5	5	5	5

where,

$$\tilde{\mathbf{\Psi}}'^{M}_{s} = \int_{\Omega_s} \mathbf{B}^T(x', z')\, \boldsymbol{\sigma}\left(x', z', t\right)\, d\Omega; \quad \tilde{\mathbf{\Psi}}'^{MT}_{s} = \int_{\Gamma_s^t} \mathbf{N}^M(x', z') \cdot \tilde{\mathbf{t}}\, d\Gamma \tag{45}$$

Γ_s^t is the part of the substrate region boundary that intersects with the Neumann boundary of the problem domain ($\Gamma_s^t \equiv \Gamma_s \cap \Gamma^t$). The microstructural displacement remains unresolved in the substrate region, Ω_s, and the stress response is a function of the macroscale displacement field only. Equation (40) constitutes the nonlinear system of equations for the evaluation of the macroscale problem. The consistent linearization and numerical evaluation algorithm for the resulting system is performed using the Newton-Raphson scheme. The linearization and numerical evaluation for HROVME is similar to the ROVME method provided in Ref. [49] and skipped herein for brevity.

5 Hourglassing Control

Based on numerical investigations on simulations without any substrate regions, we observed that the ROVME approach exhibits hourglassing behavior under certain circumstances. In this section, we demonstrate that the observed hourglassing is linked to the reduced order partitioning strategy as well as the morphology of the heterogeneous microstructure. We also indicate that this phenomenon is generally not possible for properly integrated HROVME approach.

Hourglassing is a well-known phenomenon in underintegrated finite elements, which makes possible deformation modes associated with no energy [5, 28, 26, 14]. Hourglassing is possible in the presence of rank deficiency in element stiffness matrices. In the context of 2D bilinear quadrilaterals underintegrated by a single quadrature point, the rank of the element stiffness matrix is 3, whereas a fully integrated element has a stiffness matrix of rank 5.

In the absence of inelastic effects, the element stiffness matrix for an enrichment domain using ROVME is expressed as [49]:

$$\mathbf{K}_\alpha = \sum_{\gamma=1}^{NP_\alpha} (\mathbf{B}_\gamma)^T \mathbf{S}_\gamma \tag{46}$$

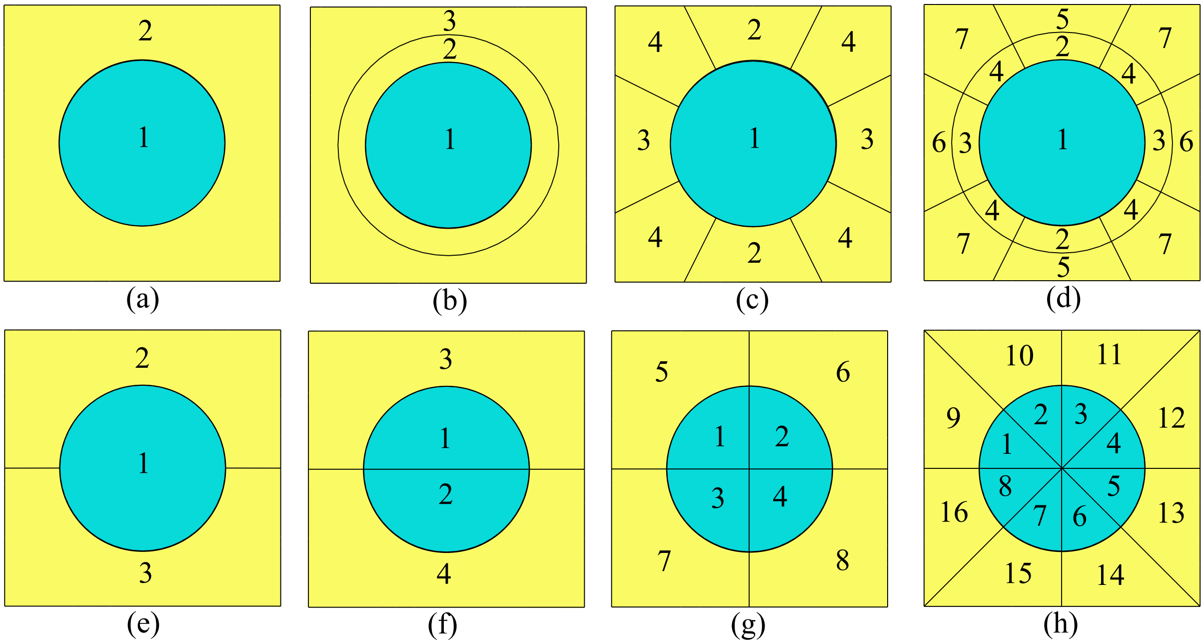

Figure 5: Partition patterns of a heterogeneous microstructure.

where,

$$\mathbf{B}_{\gamma} = \left[\int_{\Omega_{\gamma}^{\alpha}} \nabla N_A \, d\Omega \right]_{A \in [1, N_D]} \tag{47}$$

$$\mathbf{S}_{\gamma} = \left[\frac{1}{|\Omega_{\gamma}^{\alpha}|} \int_{\Omega_{\gamma}^{\alpha}} \mathbf{L} \cdot \nabla N_A + \mathbf{L} : \nabla \mathbf{H}_A^{\alpha g} \, d\Omega \right]_{A \in [1, N_D]} . \tag{48}$$

In order to demonstrate the occurrence of hourglassing in the ROVME approach, we consider a square unit cell reinforced with a single circular inclusion. The macrostructure is discretized using a single finite element that constitutes the enrichment domain. Employing eight partition patterns, the element stiffness matrix for each of them is computed by Eq. (46) and the corresponding rank is listed in Table 1. The rank deficiency occurs when the centroids of all the reduced model parts coincide with the centroid of the macroscale element (e.g, partition pattern (a)-(d)). Indeterminacy in certain deformation modes (hourglassing modes) is a direct outcome of the rank deficiency. Sufficient ranks are obtained when at least the centroid of one of the parts is not located at the center of the element (e.g, partition pattern (e)-(h)). Therefore, reduced order model partitioning, where the centroids of parts coincide, should be avoided. Some additional approaches previously employed for identifying the partitioning of the microstructure into reduced bases are discussed in Refs. [42, 43].

The hybrid integration for reduced order variational multiscale enrichment method avoids the hourglassing instabilities using Eq. (37) with $ng > 1$. Since the partition pattern of each of the microstructure, $\Theta_{\alpha g}$ ($g = 1, 2, ..., ng$), is independent of the other microstructures (as

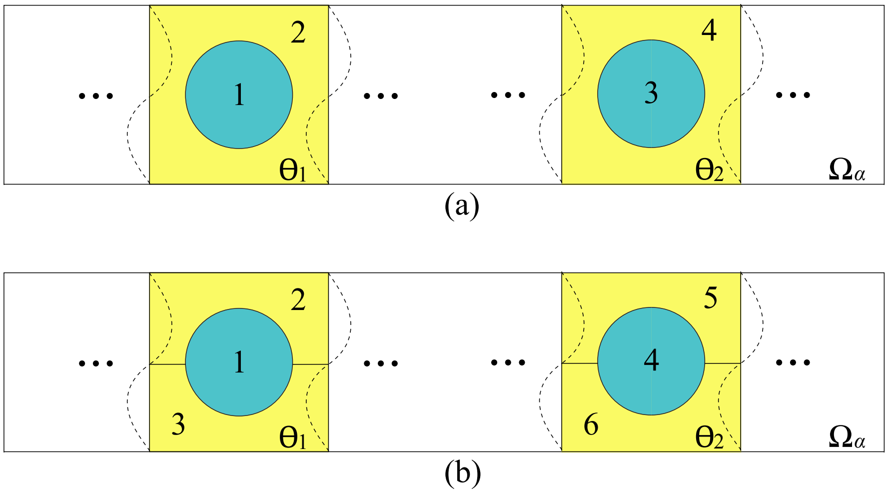

(a)

(b)

Figure 6: Partition patterns of an HROVME heterogeneous enrichment domain with $ng = 2$.

Table 2: Materials parameters for phase II material in the microstructure.

E [GPa]	ν	A [MPa]	B [MPa]
120.8	0.32	895	125
m	n	γ [MPa/second]	q
0.85	0.2	20	1.0

shown in Fig. 6 for $ng \geq 2$), it is impossible for the centroid of all parts in the enrichment domain to coincide with the center of the enrichment domain. None of the macroscale elements in Fig. 6 demonstrated the hourglassing instability issue when employed through the HROVME method.

6 Numerical Verification

The implementation of the proposed approach is verified through numerical simulations under the 2-D plane strain condition. The performance and accuracy characteristics of the hybrid multiscale integration are assessed by comparing the results with the direct ROVME method [49, 50]. The microstructure is taken to be a two-phase particulate composite with circular inclusions as shown in Fig. 7(b). Phase I (particle) is taken to be elastic with Young's modulus (E) of 395 GPa and Poisson's ratio (ν) of 0.25, where phase II matrix behaves elasto-viscoplastically. The viscoplasticity model for the matrix material relies on the Perzyna

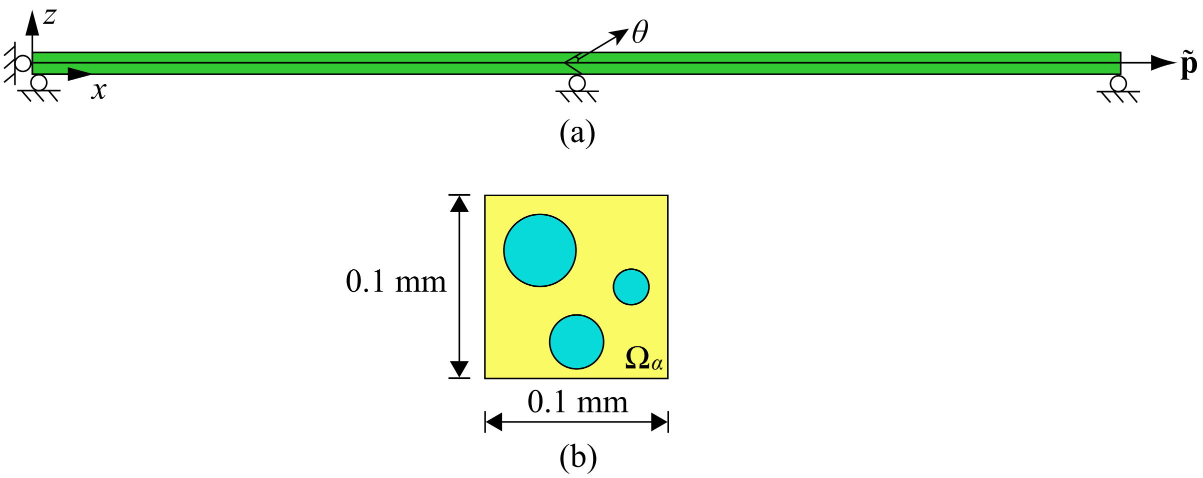

Figure 7: Model sketch and discretization of the uniaxially loaded specimens: (a) the HROVME macroscale model; and (b) the microstructure model.

formulation to describe the viscoplastic slip evolution [48]:

$$\dot{\boldsymbol{\varepsilon}}^{vp} = \gamma \left\langle \frac{f}{\sigma_y} \right\rangle^q \frac{\partial f}{\partial \boldsymbol{\sigma}} \tag{49}$$

where, γ denotes the fluidity parameter; σ_y the flow stress; q the viscoplastic hardening exponent; $\langle \cdot \rangle$ the Macaulay brackets (i.e., $\langle \cdot \rangle = ((\cdot) + |\cdot|)/2$); and f the loading function based on the classical J_2 plasticity:

$$f(\boldsymbol{\sigma}, \boldsymbol{\varepsilon}^{vp}) = \sqrt{3}\bar{\sigma} - \sigma_y(\bar{\varepsilon}^{vp}) \tag{50}$$

in which, $\bar{\sigma}$ denotes the second invariant of the deviatoric stress tensor and $\bar{\varepsilon}^{vp}$ is the effective viscoplastic strain. The flow stress is a function of the effective viscoplastic strain defined by a reduced version of the Johnson-Cook model:

$$\sigma_y = A + B(\bar{\varepsilon}^{vp})^n \tag{51}$$

where, A, B and n are material parameters. Table 2 provides the summary of the phase II material parameter values used in this section. Phase III denotes the homogenized composite used in the substrate region, the properties of which are obtained through the rule of mixtures and taken to remain elastic [11, 7]. The Young's modulus and Poisson's ratio of the homogenized substrate are 170 GPa and 0.3, respectively.

6.1 Uniaxially loaded specimens

We start by the verification of the proposed approach in the context of uniaxial loading. The macroscale problem domain and its discretization is shown in Fig. 7(a). The domain is dis-

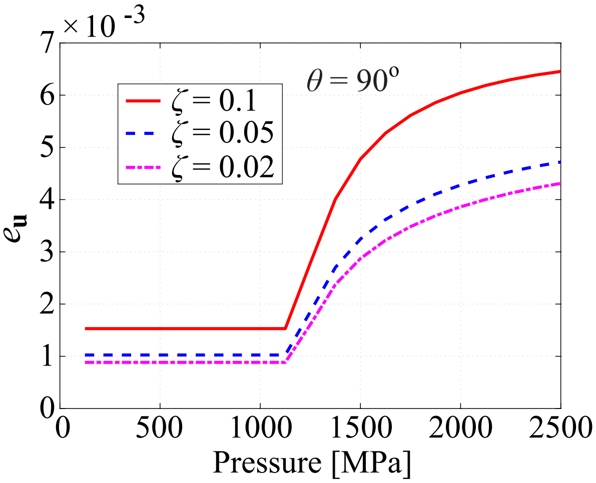

Figure 8: Errors in displacement field for the uniaxially loaded specimens with different ζ values.

cretized into 4 quadrilateral elements of high aspect ratio. Element distortion angle, θ, is used to characterize the shape of the elements. The discretization of the reference ROVME model considers a structured mesh, where each element coincides with a microstructure. The size of the microstructures is 0.1 mm×0.1 mm. The reduced order models in both the proposed and the reference ROVME methods employ a 2-part partitioning of the microstructure according to the phases. A uniform pressure load is applied on the right edge of the numerical specimens, which linearly increases from 0 to 2500 MPa in 360 seconds, at the rate of 6.94 MPa/second. The time step size employed in the simulations is 18 seconds. Further refinement of the time step size does not change the results significantly. Considering two integration points in the scale separable direction (ng=2), three HROVME specimens are tested with $\theta = 90^o$ and size scale constants of ζ=0.1, 0.05 and 0.02. As the microstructure used in the current example has a square domain in the 2D representation, the aspect ratio of an enrichment domain is the reciprocal of its size scale constant, Eqs. (9) and (10). The aspect ratios of the enrichment domains in the three HROVME specimens are 10, 20 and 50.

To investigate the accuracy of the HROVME approach compared with the reference method, the error over the enrichment region at an arbitrary time, t, is evaluated by:

$$e_\phi(t) = \frac{\sum_{\alpha=1}^{n_{\mathrm{en}}} \sum_{\gamma=1}^{NP} \left\| \phi^{\mathrm{ref}}(t) - \phi(t) \right\|_{2,\Omega_\gamma^\alpha}}{\sum_{\alpha=1}^{n_{\mathrm{en}}} \sum_{\gamma=1}^{NP} \left\| \phi^{\mathrm{ref}}(t) \right\|_{2,\Omega_\gamma^\alpha}} \tag{52}$$

where, ϕ^{ref} and ϕ denote a response field obtained from the reference (e.g., ROVME) model and the model being assessed (e.g., HROVME), respectively, with the consideration of dis-

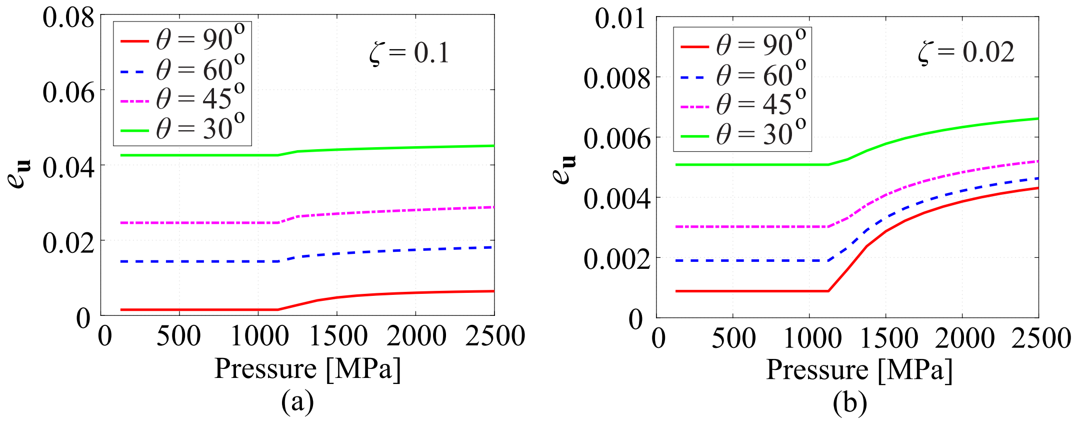

Figure 9: Errors in displacement field for the uniaxially loaded specimens with different θ and: (a) ζ=0.1; and (b) ζ=0.02.

cretization discrepancies. $\| \cdot \|_{2,\Omega_\gamma^\alpha}$ is the discrete L_2 norm of the response field computed over Ω_γ^α. Considering the ROVME model as the reference, the error in displacement field of the proposed model is presented in Fig. 8 as a function of the applied pressure amplitude and ζ. The accuracy of the proposed approach increases with decreasing ζ. This result agrees with the fundamental property that the hybrid integration scheme is weakly convergent to the reference approach at the limit $\zeta \rightarrow 0$. High accuracy is achieved for the simulations with less than 1% maximum error. For each of the specimen, the error remains constant in the elastic state (before pressure reaches 1250 MPa) and starts to accumulate at the onset of the inelastic deformation. Compared with the reference simulations, the computational time improvement of the proposed method is 6.43 times for $\zeta = 0.1$, 9.54 times for $\zeta = 0.05$ and 23.28 times for $\zeta = 0.02$.

HROVME simulations with various distortion angles, θ, are also performed. When θ=90^o, the specimen is discretized into four rectangular, undistorted, enrichment domains, while $\theta \neq 90^o$ implies distortion, with lower values indicating more significant distortion of the enrichment domains. Comparing with the ROVME method, Figure 9 presents the displacement errors of the proposed method as functions of the applied pressure amplitude, distortion and ζ. The plots indicate accuracy degradation as the angle, θ, decreases. The discretization with lower ζ is less sensitive to distortion induced accuracy degradation. The distortion effect is relatively small when $\zeta/\tan\theta \leq 0.03$.

Remark 2. The current example demonstrates the accuracy of the HROVME method compared to the ROVME method as the reference. The accuracy characteristics of the ROVME approach have been demonstrated in Refs. [49, 50]. We further demonstrate the accuracy of HROVME against the direct finite element analysis, which considers direct resolution of the microstructure throughout the problem domain. Under the strain controlled tensile load which

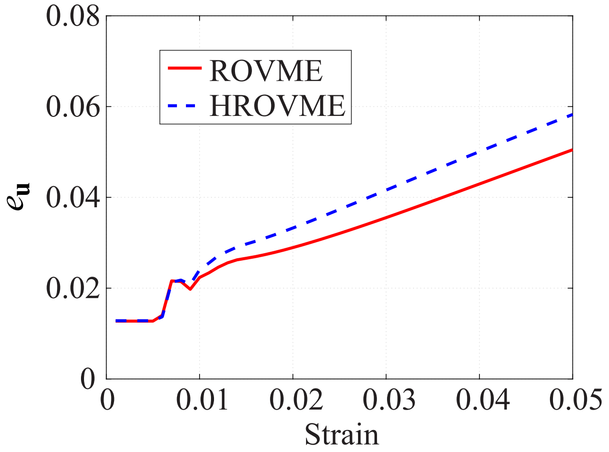

Figure 10: Errors in displacement field for the ROVME and HROVME models, comparing with the direct finite element simulation.

is linearly increased to 0.05 at the rate of 1.39×10^{-4}/second, the error in displacement field for the ROVME and HROVME models with ζ=0.1 and θ=90° are calculated from Eq. (52) and presented in Fig. 10. Figure 10 demonstrates the high accuracy of the HROVME method which follows the tendency of the error plot presented in Fig. 8. To investigate the error introduced by the proposed multiscale integration scheme, the examples in the remainder of this section all take the ROVME method as the reference.

6.2 A ring specimen

To further verify the proposed approach, the accuracy is assessed through a ring specimen under displacement controlled loading condition as shown in Fig. 11. The microstructure presented in Fig.7(b) is also considered in the current example. The inner and outer diameters of the ring are 24.46 mm and 26.46 mm, respectively. Only a quarter of the ring is modeled due to symmetry. Along the radius direction, both of the models are discretized into 10 enrichment domains. In the hoop direction, the HROVME and ROVME specimens are discretized into 20 and 200 enrichment domains, respectively. The ζ value of the HROVME enrichment domains is therefore 0.1. Along the scale separable direction, 2 integration points are employed for the hybrid integration (ng=2). All of the macroscale elements are taken as enrichment domains and their distortion is not significant ($\zeta/\tan\theta < 0.03$). The maximum amplitude of the displacement controlled load is 1 mm, at the rate of 2.8×10^{-3} mm/second. The time step size is set to 9 seconds.

The error in equivalent stress for the HROVME method compared to the reference ROVME model is plotted in Fig. 12 as a function of the magnitude of the prescribed displacement load. The specimen deforms elastically until the load reaches 0.4 mm. At the beginning of the

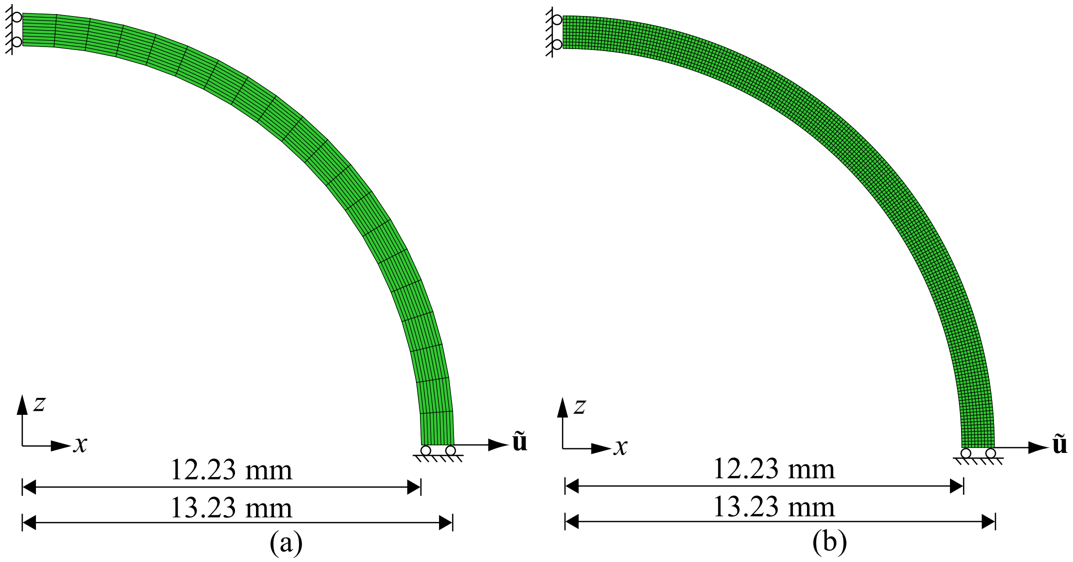

Figure 11: Model sketch and discretization of the ring specimen: (a) the HROVME macroscale model; and (b) the ROVME macroscale model.

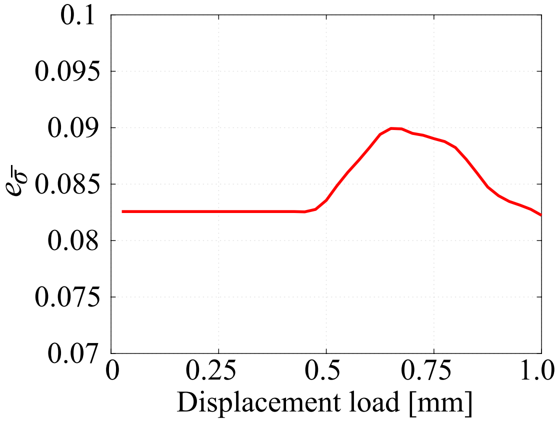

Figure 12: Error in equivalent stress for the ring specimen.

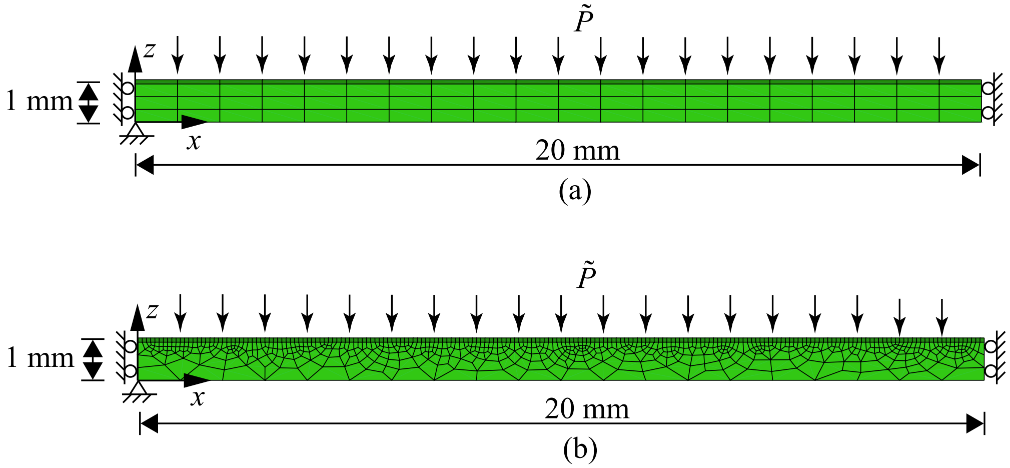

Figure 13: Model sketch and discretization of the beam specimen: (a) the HROVME macroscale model; and (b) the ROVME macroscale model.

inelastic state, the error slightly increases and then drops back as the size of the inelastic region grows in the structure. The maximum error over the simulation in terms of equivalent stress is less than 9%. The HROVME simulation is 6.07 times faster than the ROVME model which demonstrates the computational efficiency of the proposed approach.

6.3 A beam specimen

The proposed HROVME method is further verified using the numerical analysis of a beam. In this case, a substrate region is also included. A set of HROVME simulations with different number of integration points ($ng = 2, 3, 4, 5$) in the scale separable direction (x-direction in the current example) are performed to assess the accuracy characteristics of HROVME. The dimension of the specimen is 40 mm×1 mm and only half of the beam is modeled due to symmetry. The sketch and discretization of the HROVME and ROVME macroscale problems are presented in Fig. 13(a) and (b), respectively. The microstructure shown in Fig.7(b) is also employed in the current example. The HROVME macroscale model contains 80 elements of which the 20 dark elements in the top layer are taken as enrichment domains with $\zeta = 0.1$. The reference model is discretized into 755 quadrilateral macroscale elements of which the top layer of elements (200 dark shaded) are enriched. The remainder of the elements remains unenriched and modeled with the substrate material properties. A uniform pressure load is applied on the top edges of the specimens which linearly increases to 5 MPa at the rate of 1.39×10^{-2} MPa/second. The employed time step size is identical to the previous example.

Taking the ROVME method as the reference, Fig. 14 shows the equivalent stress error of the proposed HROVME method as a function of load amplitude and number of integration points employed in the scale separable direction. Similar to the previous examples, the errors are

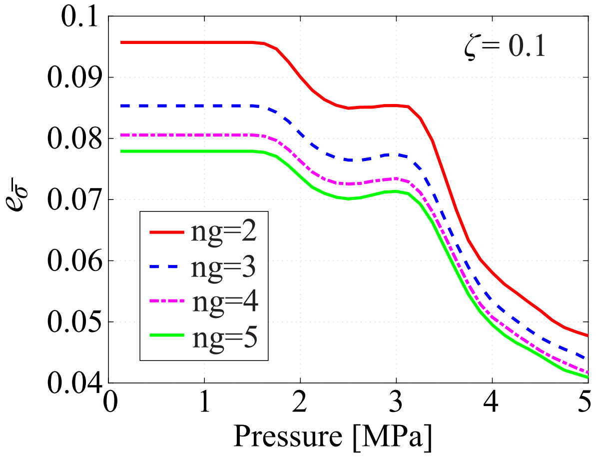

Figure 14: Errors in equivalent stress for the beam specimen with different number of integration points in the scale separable direction.

stable within the elastic state. Inelastic deformation occurs when the pressure is approximately 1.6 MPa. The results demonstrate that the accuracy of the HROVME model is enhanced by employing higher number of integration points in the scale separable direction, at the expense of higher computational cost. The computational efficiency of the proposed approach compared to the reference model are 6.95, 4.82, 3.91 and 3.5 times for ng=2, 3, 4 and 5, respectively.

7 A Coupled Transport-Thermo-Mechanical Problem

The capabilities of the proposed computational framework are demonstrated by performing a coupled transport-thermo-mechanical analysis of a stiffened skin structure. Figure 15 illustrates the geometry and loading conditions of the structure. where $\tilde{P}$ is the applied pressure amplitude, $\tilde{T}_1$ and $\tilde{T}_2$ are prescribed boundary temperatures, $\tilde{c}_0$ denotes the initial aggressive agent concentration and $\tilde{c}_\infty$ is the prescribed boundary concentration. In this example, we are interested in modeling the effect of the ingress of an aggressive environmental agent, e.g. oxygen in the current example. At high temperature, the aggressive agent ingress is modeled as Fick's diffusion. The diffusion coefficient is taken to be temperature dependent [41]:

$$D(T) = D_0 \exp\left(-\frac{Q}{RT}\right) \tag{53}$$

where, D_0=62 mm^2/second is the diffusivity at the room temperature, Q=126 kJ/mole the activation energy, R the universal gas constant and T the temperature.

---

[1] E_0 denotes the Young's modulus at the room temperature.

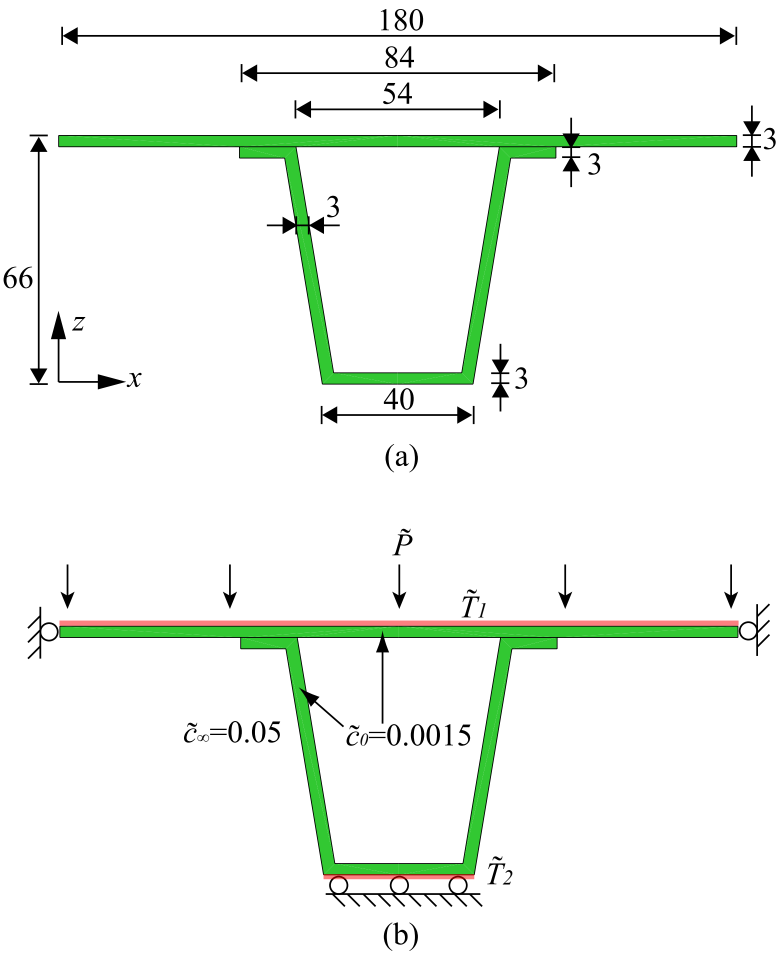

Figure 15: Model sketch of the stiffened panel specimen: (a) geometry in mm; and (b) loading conditions.

Table 3: Materials parameters for the transport-thermo-mechanical problem.

Material type	E_0 [GPa] [1]	ν	A [MPa]	B [MPa]	m
Phase I	130	0.32	600	1000	0.85
Phase II	107	0.32	350	250	0.85
Substrate	120.8	0.32	500	700	0.85
Material type	n	F [MPa]	γ[MPa/second]	q	$\alpha^T[1/^oC]$
Phase I	0.900	110	20	1.0	7.3×10^{-6}
Phase II	0.975	110	20	1.0	8.3×10^{-6}
Substrate	0.930	110	20	1.0	7.7×10^{-6}

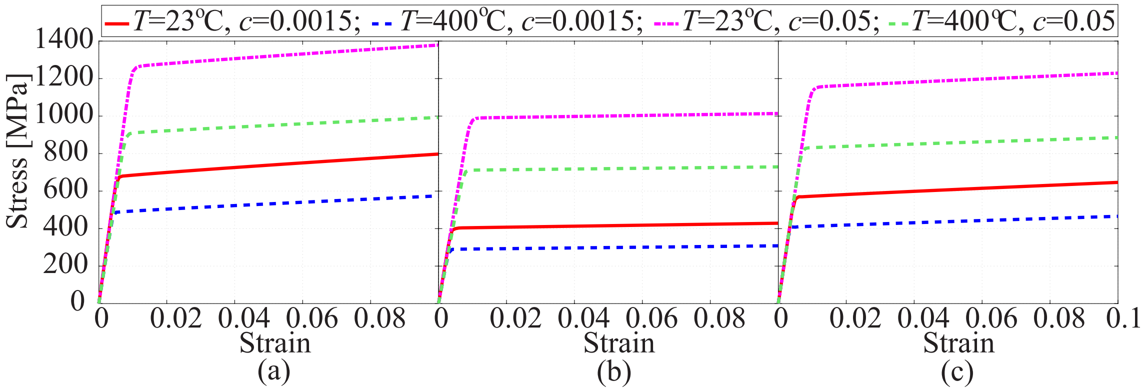

(a) (b) (c)

Figure 16: Constitutive response of the constituent materials at various temperature and aggressive agent concentration: (a) phase I; (b) phase II; and (c) substrate material.

In the context of small deformation theory, the mechanical material behavior is taken to be elasto-viscoplastic. The temperature effect on the mechanical behavior of the constituent materials is modeled through temperature dependent elastic moduli, yielding and the thermal expansion which are considered following the algorithms in Ref. [50]. The viscoplastic hardening of the constituent materials is taken to be a function of the aggressive agent concentration and temperature through the modified Johnson-Cook model as [41]:

$$\sigma_y = \left[A + B(\bar{\varepsilon}^{vp})^n + Fc\right]\left[1 - (T^*)^m\right] \tag{54}$$

where, A, B, F, m and n are material parameters; c the aggressive agent concentrate and T^* the non-dimensional temperature:

$$T^* = \frac{T - T_{\text{room}}}{T_{\text{melt}} - T_{\text{room}}} \tag{55}$$

in which, T_{room} and T_{melt} are the room and melting temperatures, respectively. A two-phase microstructure is considered for the material. The material properties of the constituent materials are listed in Table 3. The Young's moduli of the materials linearly vary as a function of temperature with 0.0381 GPa/°C, 0.0314 GPa/°C and 0.0354 GPa/°C for phases I and II, and the substrate materials. The properties of the substrate material are obtained through mixture theory. At 0.056/second of strain loading rate, the constitutive responses of the constituent materials under various temperature and concentration conditions are plotted in Fig. 16.

First, the top and bottom surfaces of the structure are exposed to 400°C and 150°C, which results in a non-uniform temperature distribution over the structure as shown in Fig. 17. In this analysis, the temperature distribution is obtained from a direct finite element simulation of the classical steady state heat conduction (i.e., Ficks law) using a very fine discretization

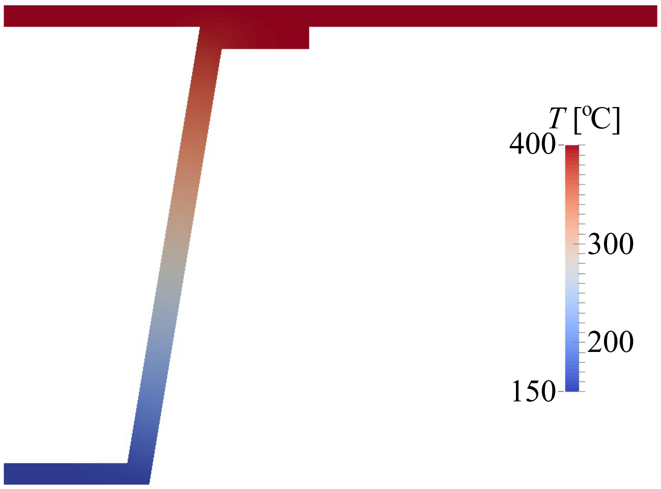

Figure 17: Temperature contour of the stiffened panel specimen.

near the surfaces of the structure. In view of random distribution of the phases within the microstructure, the steady state temperature field is approximated as uniform over the fine scale and the microstructural heterogeneity is not resolved. Next, prescribing the resulting steady state temperature field, aggressive agents then ingress into the structure resulting in a non-uniform distribution of concentrations as shown in Fig. 18 after an exposure duration of 50 hours. Along the surfaces of the panel and the hat stiffener, the aggressive agent diffuses into the structure due to the induced concentration gradients. The region near the hot boundary has significant diffusion whereas the region near the cool surface does not exhibit significant diffusion. The detailed concentration distribution as a function of the distance to the ambient surface is plotted in Fig. 19 for near hot and cold surfaces. Last, the structure is subjected to a pressure load which linearly increases to 5 MPa, under the prescribed temperature and concentration distributions.

In order to capture the effect of the aggressive agent on the structural behavior, two layers of enrichment domains are embedded along the surfaces of the specimen as illustrated in Fig. 20. The thickness of each layer is 0.5 mm. A two-phase microstructure, as shown in Fig. 21, is used within the enrichment domains. Phase I and Phase II materials are identified as dark and light elements, respectively. The microstructure is discretized into 20 parts, 2 parts associated with the phases in each of the 10 layers. The number of integration points in the scale separable direction of the the hybrid integration is 2 (ng=2). In view of the size of the structure, direct resolution of each microstructure along the surface region is computationally prohibitive and the reference approach is not employed in this study. Three cases of loading conditions are investigated to assess the effect of field coupling on the mechanical response including (a) a transport-thermo-mechanical case, (b) a thermo-mechanical case without considering aggressive agent ingress and (c) a pure mechanical case at room temperature.

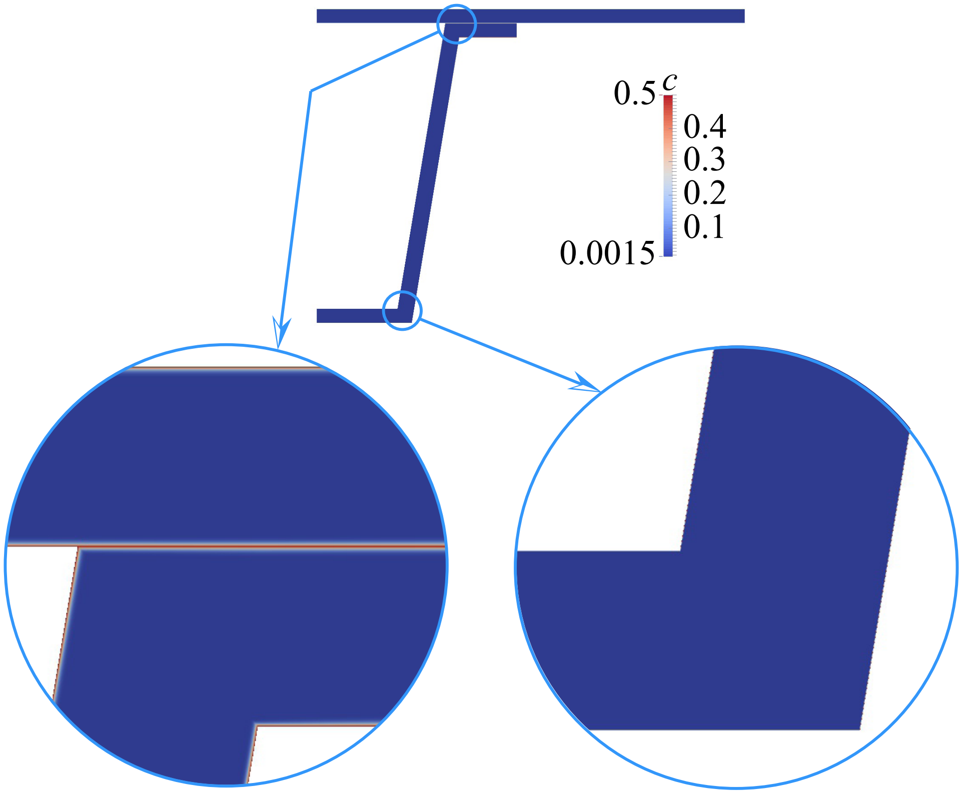

Figure 18: Aggressive agent concentration contour of the stiffened panel specimen.

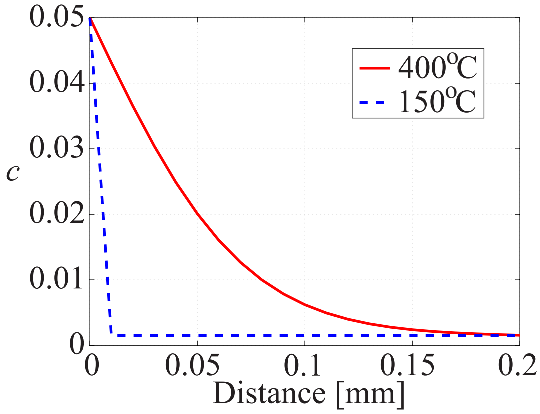

Figure 19: Aggressive agent concentration distributions along with the distance to the ambient surface.

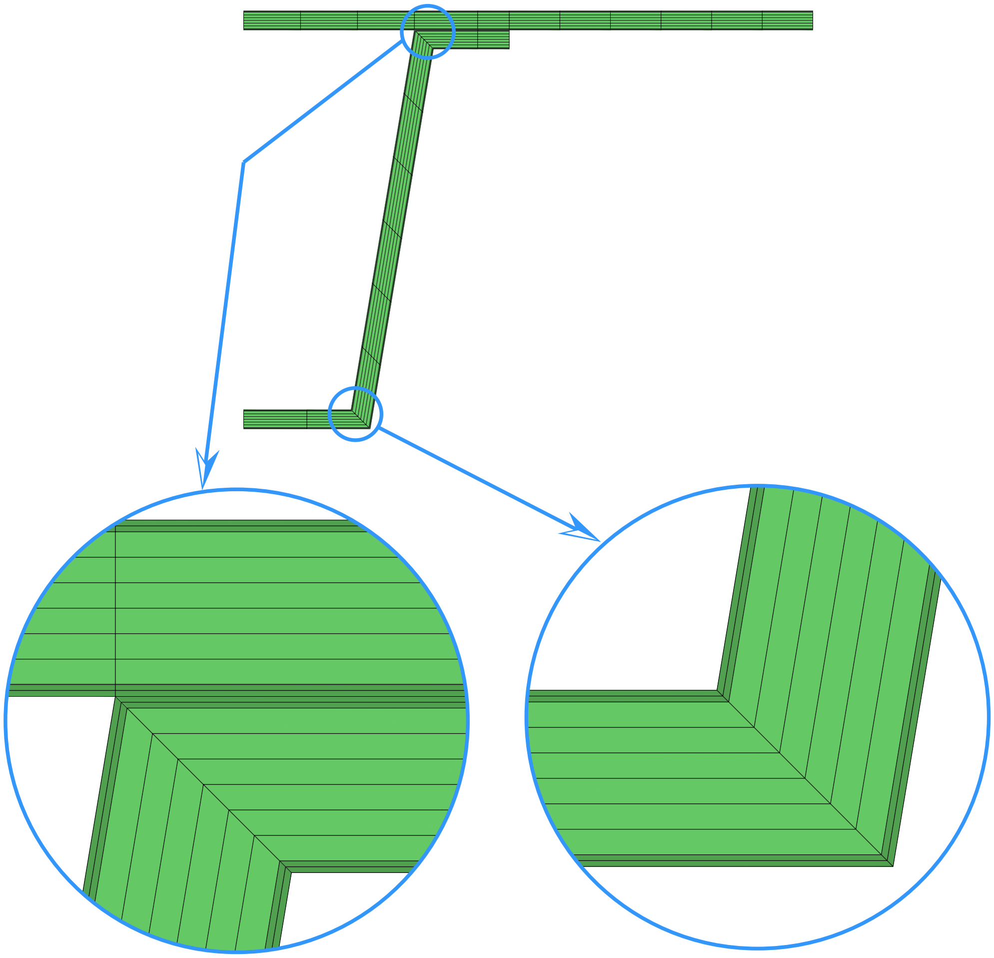

Figure 20: Macroscale discretization of the HROVME model.

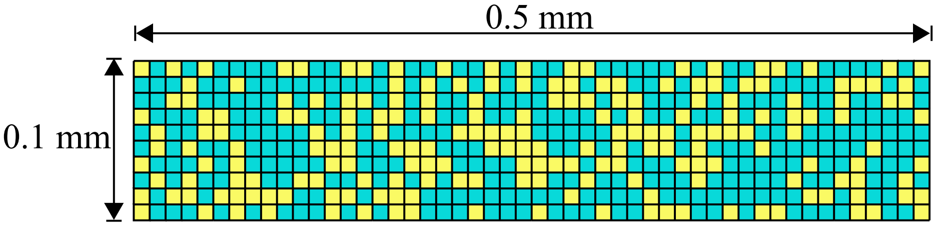

Figure 21: Resolved microstructure of the HROVME model.

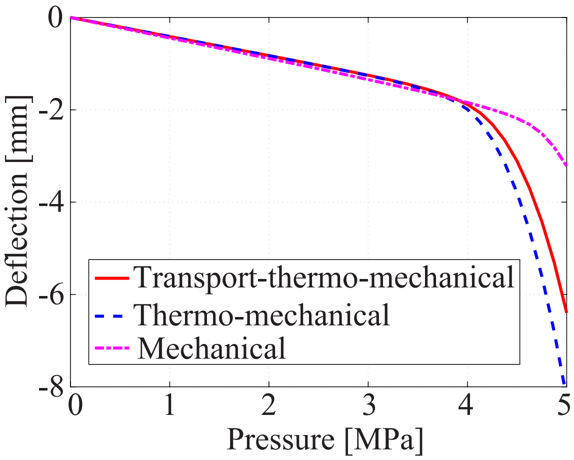

Figure 22: Center deflections along with pressure load.

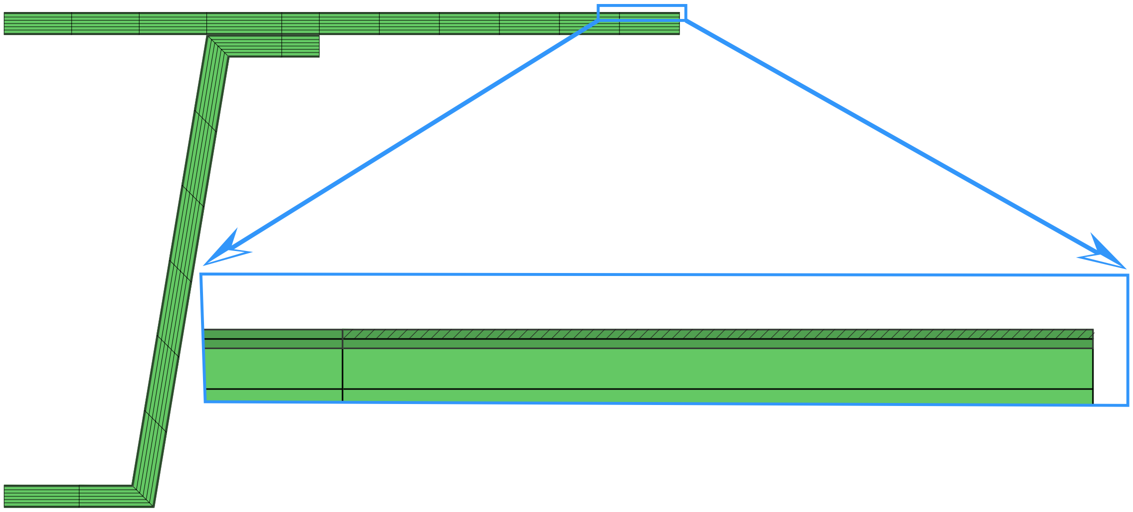

Figure 23: Location of the critical enrichment domain (dashed).

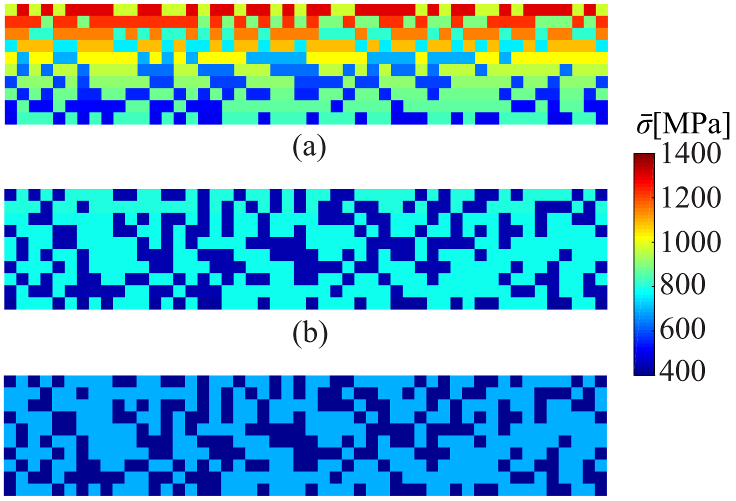

(a)

(b)

(c)

Figure 24: Stress countours of the critical microstructure for specimen subjected to: (a) transport-thermo-mechanical loads; (b) thermo-mechanical loads; and (c) only mechanical load.

Figure 22 shows the deflection of the center of the stiffened panel for the three cases as a function of applied load. When contrasting cases (b) and (c), the presence of high temperature clearly reduces the overall stiffness of the structure and induces inelastic deformations with notably larger magnitudes. In the presence of aggressive agent ingress, case (a), the specimen exhibits a clearly stiffer response than case (b). We note that although diffusion affects the structure along a narrow surface region, the deflection change in the inelastic stage is significant. Maximum stress is contained by the critical enrichment domain right next to the top center point of the panel. The location of the critical enrichment domain in the structure is identified as the dashed element which is shown in Fig. 23. The local equivalent stress distribution within the microstructure of the critical enrichment domain is presented in Fig. 24 for all three simulations. For plotting purposes, the microstructural stress distributions are reconstructed over the microstructure during post-processing. The plots indicate uniform stress distribution over the parts of the microstructure consistent with the reduced order approximation. The transport-thermo-mechanical specimen, case (a), demonstrates significantly higher equivalent stress due to the ingress effect and high temperature induced expansion. More importantly, the HROVME method has the capability of capturing the stress gradient induced by the aggressive agent concentration variation across the thickness of the enrichment domain, as shown in Fig. 24(a). In the absence of aggressive agent, the local responses of the thermo-mechanical and mechanical simulations (Figs. 24(b) and (c)) exhibit more uniform stress distributions within the microstructure.

8 Conclusions

This manuscript presented a new hybrid multiscale integration scheme for directionally scale separable multiscale problems. The proposed approach is particularly suitable for structural problems, where surface degradation and embrittlement effects are critical to the overall response. The proposed hybrid multiscale integration algorithm was applied to arrive at a reduced order multiscale variational multiscale enrichment model (HROVME), which demonstrates significant computational efficiency and reasonable accuracy. The investigations in the current manuscript are limited to the viscoplastic behavior within the material constituents. Surface degradation problems are typically associated with early onset of microcracking that changes the stress distributions within the surface region affected by the aggressive agent. Future investigations must therefore focus on the extension of the proposed multiscaling algorithm to account for the nucleation and growth of microcracks within the enrichment domains. This poses significant challenges in terms of the enforcement of appropriate boundary conditions for the microscale problem, as well as the model order reduction of a microstructure that evolves as a function of the load state.

9 Acknowledgements

The authors gratefully acknowledge the research funding from the Air Force Office of Scientific Research Multi-Scale Structural Mechanics and Prognosis Program (Grant No: FA9550-13-1-0104. Program Manager: Dr. Jaimie Tiley). We also acknowledge the technical cooperation of the Structural Sciences Center at the Air Force Research Laboratory.

References

[1] T. Arbogast. Implementation of a locally conservative numerical subgrid upscaling scheme for two-phase Darcy flow. *Comput. GeoSci.*, 6:453–481, 2002.

[2] T. Arbogast. Analysis of a two-scale, locally conservative subgrid upscaling for elliptic problems. *SIAM J. on Numer. Anal.*, 42:576–598, 2004.

[3] I. Babuska. *Homogenization and application: mathematical and computational problems, in: B. Hubbard (Ed.), Numerical Solution of Partial Differential Equations - III.* SYNSPADE, New York, 1975.

[4] Y. A. Bahei-El-Din, A. M. Rajendran, and M. A. Zikry. A micromechanical model for

damage progression in woven composite systems. *Int. J. Solids Structures*, 41:2307–2330, 2004.

[5] T. Belytschko, J. S.-J. Ong, W. K. Liu, and J. M. Kennedy. Hourglass control in linear and nonlinear problems. *Comput. Methods Appl. Mech. Engrg.*, 43:251–276, 1984.

[6] A. Bensoussan, J-L. Lions, and G. Papanicolau. *Asymptotic Analysis for Periodic Structures.* Elsevier, 1978.

[7] D. Bettge, B. Gunther, W. Wedell, P.D. Portella, J. Hemptenmacher, P.W.M. Peters, and B. Skrotzki. Mechanical behavior and fatigue damage of a titanium matrix composite reinforced with continuous SiC fibers. *Mater. Sci. Eng., A*, 452-453:536–544, 2007.

[8] S. Bhattacharjee and K. Matous. A nonlinear manifold based reduced order model for multiscale analysis of heterogeneous hyperelastic materials. *J. Comput. Phys.*, 313:635–653, 2016.

[9] F. Bignonnet, K. Sab, L. Dormieux, S. Brisard, and A. Bisson. Macroscopically consistent non-local modeling of heterogeneous media. *Comput. Methods Appl. Mech. Engrg.*, 278: 218–238, 2014.

[10] F. Brezzi, L. P. Franca, T. J. R. Hughes, and A. Russo. $b = \int g$. *Comput. Methods Appl. Mech. Engrg.*, 145:329–339, 1997.

[11] N. Carrere, D. Boivin, R. Valle, and A. Vassel. Local texture measurements in a SiC/Ti composite manufactured by the foil-fiber-foil. *Scripta Mater.*, 44:867–872, 2001.

[12] J. L. Chaboche, S. Kruch, J. F. Maire, and T. Pottier. Towards a micromechanics based inelastic and damage modeling of composites. *Int. J. Plasticity*, 17:411–439, 2001.

[13] D. Cioranescu and P. Donato. *An Introduction to Homogenization.* Oxford University Press, 1999.

[14] R. D. Cook, D. S. Malkus, M. E. Plesha, and R. J. Witt. *Concepts and Applications of Finite Element Analysis, 4th Edition.* John Wiley & Sons. Inc., 2002.

[15] C. A. Duarte and D. J. Kim. Analysis and applications of a generalized finite element method with global–local enrichment functions. *Comput. Methods Appl. Mech. Engrg.*, 197:487–504, 2008.

[16] G. J. Dvorak. Transformation field analysis of inelastic composite materials. *Proc. R. Soc. Lond. A*, 437:311–327, 1992.

[17] W. E, P. Ming, and P. Zhang. Analysis of the heterogeneous multiscale method for elliptic homogenization problems. *J. Am. Math. Soc.*, 18:121–156, 2004.

[18] Y. Efendiev, J. Galvis, and T. Hou. Generalized multiscale finite element methods. *J. Comput. Phys.*, 251:116–135, 2013.

[19] A. G. Evans, F.W. Zok, R. M. McMeeking, and Z. Z. Du. Models of high temperature, environmentally assisted embrittlement in ceramic matrix composites. *J. Am. Ceram. Soc.*, 79:2345–2352, 1996.

[20] J. Fish. The s-version of the finite element method. *Computers & Structures*, 43:539–547, 1992.

[21] J. Fish and S. Markolefas. Adaptive global-local refinement strategy based on the interior error estimates of the h-method. *Int. J. Numer. Meth. Engng.*, 37:827–838, 1994.

[22] L. Gendre, O. Allix, P. Gosselet, and F. Comte. Non-intrusive and exact global/local techniques for structural problems with local plasticity. *Comput. Mech.*, 44:233–245, 2009.

[23] J. M. Guedes and N. Kikuchi. Preprocessing and postprocessing for materials based on the homogenization method with adaptive finite element methods. *Comput. Methods Appl. Mech. Engrg.*, 83:143–198, 1990.

[24] T. Y. Hou and X. Wu. A multiscale finite element method for elliptic problems in composite materials and porous media. *J. Comput. Phys.*, 134:169–189, 1997.

[25] T. J. R. Hughes. Multiscale phenomena: Green's functions, the Dirichlet-to-Neumann formulation, subgrid scale models, bubbles and the origins of stabilized methods. *Comput. Methods Appl. Mech. Engrg.*, 127:387–401, 1995.

[26] T. J. R. Hughes. *The Finite Element Method: Linear Static and Dynamic Finite Element Analysis.* Prentice-Hall, Inc. Englewood Cliffs, N. J., 2000.

[27] T. J. R. Hughes, G. R. Feijoo, and J. B. Quincy. The variational multiscale method - a paradigm for computational mechanics. *Comput. Methods Appl. Mech. Engrg.*, 166:3–24, 1998.

[28] O. P. Jacquotte and J. T. Oden. Analysis of hourglass instabilities and control in underintegrated finite element methods. *Comput. Methods Appl. Mech. Engrg.*, 44:339–363, 1984.

[29] A. Levy and Y.-F. Man. Surface degradation of ductile metal in elevated temperature gas-particle streams. *Wear*, 111:173–186, 1986.

[30] O. Lloberas-Valls, D. J. Rixen, A. Simone, and L. J. Sluys. Domain decomposition techniques for the efficient modeling of brittle heterogeneous materials. *Comput. Methods Appl. Mech. Engrg.*, 200:1577–1590, 2011.

[31] K. M. Mao and C. T. Sun. A refined global-local finite element analysis method. *Int. J. Numer. Meth. Engng.*, 32:29–43, 1991.

[32] J.C. Michel and P. Suquet. Computational analysis of nonlinear composite structures using the nonuniform transformation field analysis. *Comput. Methods Appl. Mech. Engrg.*, 193:5477–5502, 2004.

[33] H. Moulinec and P. Suquet. A numerical method for computing the overall response of nonlinear composites with complex microstructure. *Comput. Methods Appl. Mech. Engrg.*, 157:69–94, 1998.

[34] A. K. Noor. Global-local methodologies and their application to nonlinear analysis. *Finite Elements Anal. Des.*, 2:333–346, 1986.

[35] P. O' Hara, C. A. Duarte, T. Eason, and J. Garzon. Efficient analysis of transient heat transfer problems exhibiting sharp thermal gradients. *Comput. Mech.*, 51:743–764, 2013.

[36] J. Oliver, M. Caicedo, A.E. Huespe, J.A. Hernandez, and E. Roubin. Reduced order modeling strategies for computational multiscale fracture. *Comput. Meth. Appl. Mech. Engng,*, 313:560–595, 2017.

[37] R. A. Oriani. Hydrogen embrittlement of steels. *Ann. Rev. Mater. Sci.*, 8:327–357, 1978.

[38] C. Oskay. Variational multiscale enrichment for modeling coupled mechano-diffusion problems. *Int. J. Numer. Meth. Engng.*, 89:686–705, 2012.

[39] C. Oskay. Variational multiscale enrichment method with mixed boundary conditions for modeling diffusion and deformation problems. *Comput. Methods Appl. Mech. Engrg.*, 264: 178–190, 2013.

[40] C. Oskay and J. Fish. Eigendeformation-based reduced order homogenization for failure analysis of heterogeneous materials. *Comput. Methods Appl. Mech. Engrg.*, 196:1216–1243, 2007.

[41] C. Oskay and M. Haney. Computational modeling of titanium structures subjected to thermo-chemo-mechanical environment. *Int. J. Solids Struct.*, 47:3341–3351, 2010.

[42] P. A. Sparks and C. Oskay. Identification of optimal reduced order computational models for failure of heterogeneous materials. *Int. J. Mult. Comp. Eng.*, 11:185–200, 2013.

[43] P. A. Sparks and C. Oskay. The method of failure paths for reduced-order computational homogenization. *Int. J. Mult. Comp. Eng.*, 14:515–534, 2016.

[44] S. P. Walker and B. J. Sullivan. Sharp refractory composite leading edges on hypersonic vehicles. *AIAA 20036915, Proceedings of the 12th AIAA International Space Planes and Hypersonic Systems and Technologies, 1519 December 2003, Norfolk, VA.*, 2003.

[45] R.G. Wellman and J.R. Nicholls. High temperature erosion-oxidation mechanisms, maps and models. *Wear*, 256:907917, 2004.

[46] H. Yan and C. Oskay. A viscoelastic-viscoplastic model of titanium structures subjected to thermo-chemo-mechanical environment. *Int. J. Solids Struct.*, 56-57:29–42, 2015.

[47] J. Yvonnet and Q.-C. He. The reduced model multiscale method (R3M) for the non-linear homogenization of hyperelastic media at finite strains. *J. Comput. Phys.*, 223:341–368, 2007.

[48] S. Zhang and C. Oskay. Variational multiscale enrichment method with mixed boundary conditions for elasto-viscoplastic problems. *Comput. Mech.*, 55:771–787, 2015.

[49] S. Zhang and C. Oskay. Reduced order variational multiscale enrichment method for elasto-viscoplastic problems. *Comput. Methods Appl. Mech. Engrg.*, 300:199–224, 2016.

[50] S. Zhang and C. Oskay. Reduced order variational multiscale enrichment method for thermo-mechanical problems. *Comput. Mech.*, 59:887–907, 2017.

A Appendix

This appendix presents the algorithm for analytically obtaining the coefficient tensors, $\mathbf{B}_{\gamma A}^{\alpha g}$ and $\mathbf{S}_{\gamma A}^{\alpha g}$, of enrichment domains with different ζ values. For the clarity of presentation, the bold symbol in this section denotes vector notation.

First, the coefficient tensors are obtained for an enrichment domain with ζ_{ref}. Then, following the evaluation procedure of the coefficient tensors (Eqs. (24), (30) and (38)), the relationships of the coefficient tensors between enrichment domains with ζ and ζ_{ref} are obtained as:

$$\mathbf{B}_{\gamma Aij}^{\alpha g}(\zeta) = \mathbf{T}_{ij}^{\text{B}}(\zeta, \zeta_{\text{ref}})\ \mathbf{B}_{\gamma Aij}^{\alpha g}(\zeta_{\text{ref}}) \tag{56}$$

$$\mathbf{S}_{\gamma Aij}^{\alpha g}(\zeta) = \mathbf{T}_{ij}^{\text{S}}(\zeta, \zeta_{\text{ref}})\ \mathbf{S}_{\gamma Aij}^{\alpha g}(\zeta_{\text{ref}}) \tag{57}$$

where, the components of $\mathbf{T}^{\text{B}}$ and $\mathbf{T}^{\text{S}}$ for 2-D problems are:

$$\mathbf{T}^{\text{B}}(\zeta, \zeta_{\text{ref}}) = \begin{bmatrix} \frac{\zeta}{\zeta_{\text{ref}}} & 1 \\ 1 & 1 \\ 1 & \frac{\zeta}{\zeta_{\text{ref}}} \end{bmatrix} \tag{58}$$

$$\mathbf{T}^{\text{S}}(\zeta, \zeta_{\text{ref}}) = \begin{bmatrix} \frac{\zeta}{\zeta_{\text{ref}}} & 1 \\ \frac{\zeta}{\zeta_{\text{ref}}} & 1 \\ 1 & \frac{\zeta}{\zeta_{\text{ref}}} \end{bmatrix} \tag{59}$$